






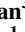

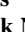



RESEARCH ARTICLE

10.1029/2023JD040650

Synoptic Analysis and WRF-Chem Model Simulation of Dust Events in the Southwestern United States

Special Collection:

Dust and dust storms: From physical processes to human health, safety, and welfare

Saroj Dhital¹ , Nicholas P. Webb¹ , Adrian Chappell² , Michael L. Kaplan³ , Travis W. Nauman⁴, Gayle Tyree⁵, Michael C. Duniway⁵ , Brandon Edwards¹ , Sandra L. LeGrand⁶ , Theodore W. Letcher⁷, S. McKenzie Skiles⁸ , Patrick Naple⁸, Nathaniel W. Chaney⁹ , and Jiaxuan Cai⁹

Key Points:

- Large-scale meteorological analysis and dust emission and transport simulation of Southwest US dust-on-snow events
- Polar and Sub-tropical jet stream interaction was a common upper-level meteorological feature to Southwest US dust events
- Simulated dust source areas on the Colorado Plateau and Chihuahuan Desert reflect observed dust emission hot spots

Supporting Information:

Supporting Information may be found in the online version of this article.

Correspondence to:

S. Dhital,
sdhital@nmsu.edu

Citation:

Dhital, S., Webb, N. P., Chappell, A., Kaplan, M. L., Nauman, T. W., Tyree, G., et al. (2024). Synoptic analysis and WRF-Chem model simulation of dust events in the southwestern United States. *Journal of Geophysical Research: Atmospheres*, 129, e2023JD040650. <https://doi.org/10.1029/2023JD040650>

Received 22 DEC 2023

Accepted 19 MAY 2024

© 2024 The Author(s). This article has been contributed to by U.S. Government employees and their work is in the public domain in the USA.

This is an open access article under the terms of the [Creative Commons Attribution License](https://creativecommons.org/licenses/by/4.0/), which permits use, distribution and reproduction in any medium, provided the original work is properly cited.

¹USDA-ARS Jornada Experimental Range, Las Cruces, NM, USA, ²School of Earth and Environmental Sciences, Cardiff University, Cardiff, UK, ³Division of Atmospheric Sciences, Desert Research Institute, Reno, NV, USA, ⁴USDA-NRCS National Soil Survey Center, Lincoln, NE, USA, ⁵U.S. Geological Survey, Southwest Biological Science Center, Moab, UT, USA, ⁶U.S. Army Engineer Research and Development Center, Geospatial Research Laboratory, Alexandria, VA, USA, ⁷U.S. Army Engineer Research and Development Center, Cold Regions Research and Engineering Laboratory, Hanover, NH, USA, ⁸Department of Geography, University of Utah, Salt Lake City, UT, USA, ⁹Department of Civil and Environmental Engineering, Duke University, Durham, NC, USA

Abstract Dust transported from rangelands of the Southwestern United States (US) to mountain snowpack in the Upper Colorado River Basin during spring (March–May) forces earlier and faster snowmelt, which creates problems for water resources and agriculture. To better understand the drivers of dust events, we investigated large-scale meteorology responsible for organizing two Southwest US dust events from two different dominant geographic locations: (a) the Colorado Plateau and (b) the northern Chihuahuan Desert. High-resolution Weather Research and Forecasting coupled with Chemistry model (WRF-Chem) simulations with the Air Force Weather Agency dust emission scheme incorporating a MODIS albedo-based drag-partition was used to explore land surface-atmosphere interactions driving two dust events. We identified commonalities in their meteorological setups. The meteorological analyses revealed that Polar and Sub-tropical jet stream interaction was a common upper-level meteorological feature before each of the two dust events. When the two jet streams merged, a strong northeast-directed pressure gradient upstream and over the source areas resulted in strong near-surface winds, which lifted available dust into the atmosphere. Concurrently, a strong mid-tropospheric flow developed over the dust source areas, which transported dust to the San Juan Mountains and southern Colorado snowpack. The WRF-Chem simulations reproduced both dust events, indicating that the simulations represented the dust sources that contributed to dust-on-snow events reasonably well. The representativeness of the simulated dust emission and transport in different geographic and meteorological conditions with our use of albedo-based drag partition provides a basis for additional dust-on-snow simulations to assess the hydrologic impact in the Southwest US.

Plain Language Summary Dust transported from rangelands of the Southwestern United States (US) to the mountain snowpack in the Upper Colorado River Basin during spring (March–May) is a growing problem for water resources and agriculture. Understanding the drivers of dust events is essential to better forecast the possible impact of dust on water resources. We investigated the weather conditions that led to two dust events originating from the Colorado Plateau and northern Chihuahuan Desert. We also performed computer simulations with an improved dust emission model to explore the influence of vegetation on the susceptibility of landscapes to wind erosion during dust events. Our meteorological analysis revealed commonalities in the upper-level meteorology before dust event formation and provided valuable insights into where and when high-impact dust events may occur. However, further investigation is needed to generalize the impact of jet stream interaction on dust events' intensity. Our simulations represented the dust sources reasonably well by using an improved dust emission model. The improved dust emission and transport simulation under different meteorological and geographical conditions provided a basis for future dust-on-snow simulations to assess the hydrological impact in the Southwestern US.

1. Introduction

In spring (March–May), dust events across the Southwestern United States (hereafter Southwest) bring deleterious impacts on human health by degrading air quality (Achakulwisut et al., 2017; Hand et al., 2017, 2019);

regional transportation by reducing visibility (Tong et al., 2023); ecosystem services and agricultural production by losing topsoil and associated nutrients and soil carbon (Duniway et al., 2019; Webb et al., 2017); and water resources by impacting dust radiative forcing of snow melt (Rahimi et al., 2020; Skiles & Painter, 2017). Dust transported from regionally active source areas affects mountain snowpack in the Upper Colorado River Basin (Skiles et al., 2015). Deposited dust changes snow properties (e.g., Skiles & Painter, 2018), accelerates snow melt (e.g., Skiles et al., 2015), and alters the hydrological cycle in the greater Colorado River Basin (CRB) (e.g., Painter et al., 2010) and Rio Grande Basin (RGB), the main water resources for more than 40 million people across the Southwest. Agriculture in the CRB generates US\$60 billion each year that is dependent on 90% of water resources in the basin (Thiel, 2013), and the RGB supports a US\$1 billion agricultural sector dependent on 85% of the basin's water resources annually (Kort, 2013), with both basins being important international sources of irrigation water. Therefore, accurately predicting dust events is essential for forecasting the impacts of dust on the hydrological cycle for land and water management, agriculture, and livelihoods.

The Weather Research and Forecasting model (WRF; Skamarock et al., 2019) and WRF with Chemistry (WRF-Chem; Grell et al., 2005) are numerical models that simulate meteorological processes and atmospheric chemistry. WRF-Chem has a long history of being used as a tool to support studies of dust emission and atmospheric transport (e.g., Dhital et al., 2021; Parajuli et al., 2019; Solomos et al., 2018; Zhao et al., 2010). Convection-permitting WRF-Chem model simulations have been increasingly used to investigate the role of meteorology in organizing strong dust events and to assess impacts of transported dust (e.g., Adhikari & Mejia, 2022; Dhital et al., 2020, 2021; Evan et al., 2022; LeGrand et al., 2023; Rahimi et al., 2020; Solomos et al., 2018). These higher resolution simulations are useful because they can resolve the mesoscale weather features and complex terrain that control near surface winds over dust sources (e.g., Evan et al., 2022; LeGrand et al., 2023; Solomas et al., 2018). WRF-Chem has also been used as a tool to study the effect of dust on snow in the CRB (Oaida et al., 2015).

Currently, three dust emission schemes can be employed in the WRF-Chem model to simulate dust emission: the Goddard Global Ozone Chemistry Aerosol Radiation and Transport (GOCART); the Air Force Weather Agency (AFWA); and the University of Cologne scheme (UoC; see LeGrand et al., 2019) for a full description and baseline comparisons). A requirement for these dust emission schemes to accurately predict dust events impacting the CRB and RGB is to represent surface roughness, especially vegetation, and its spatiotemporal change. All three dust emission schemes, as implemented in WRF-Chem, incorporate a static mask designed to block dust emission from vegetated areas derived from a relatively coarse, 1-degree resolution land cover data set (LeGrand et al., 2019). The AFWA dust emission scheme further restricts dust emission from areas where the aerodynamic roughness length is > 20 cm. This setting effectively limits dust emission in the AFWA scheme to barren, cropland, savanna, grassland, or shrubland areas. The UoC scheme is the only dust emission scheme in WRF-Chem that includes some form of dynamic roughness effects on dust emission by using a form of the drag partition scheme developed by Raupach (1992). However, the UoC module estimates roughness conditions from monthly greenness fraction climatology data sets, which can lead to poor simulation outcomes under variable climate regimes (e.g., LeGrand et al., 2019).

Recently, LeGrand et al. (2023) incorporated the albedo-based drag partition (Chappell & Webb, 2016; hereafter CW16) into the AFWA dust emission scheme to represent the effects of vegetation and other non-erodible roughness elements on the wind shear velocity that drives dust emission. The albedo-based approach, which partitions drag of different scales of roughness (e.g., vegetation, rocks), may be implemented using Moderate Resolution Imaging Spectroradiometer (MODIS) land surface albedo data and either a bi-directional reflectance distribution function (BRDF) parameter or nadir BRDF adjusted reflectance (Chappell et al., 2018). LeGrand et al. (2023) demonstrated significant improvements in a simulation with the CW16 model over the original AFWA scheme for a Southwestern summertime convective dust event.

Synoptically-forced spring dust events are a common type of dust event in the Southwest and are thought to be the main driver of dust-on-snow events (Lei & Wang, 2014). We investigated large-scale meteorological conditions of two spring-season Southwest dust events originating in the two dominants, and geographically different, dust source areas of the Southwest. We then simulated the dust events using the WRF-Chem model following a similar approach to LeGrand et al. (2023) with the objective being to resolve the land surface-atmosphere interactions producing dust and how dust source area dynamics may be influencing dust emissions across the Southwest. Although the primary focus of this study is the numerical simulation of dust events, we purposefully added large-scale meteorological analyses to investigate upper-level meteorological precursors that drive dust events.

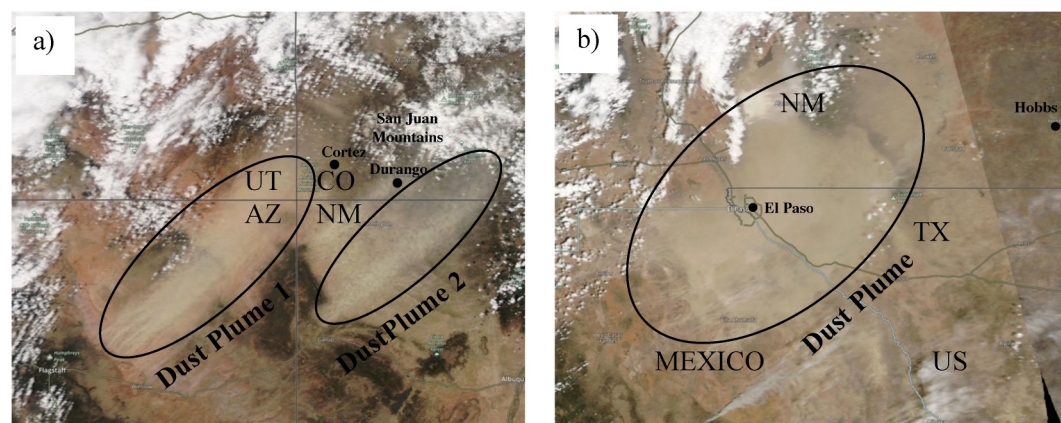


Figure 1. True-color image from MODIS-Aqua (a) 2013-04-16 and (b) 2017-03-23. Dust clouds appear brownish gray. Images were obtained from the National Aeronautics and Space Administration (NASA) Worldview platform (NASA Worldview, 2022).

2. Brief Description of Dust Events

We simulated two spring dust events: (a) April 16–17, 2013 (A13) over the Colorado Plateau (CP) and (b) March 23–24, 2017 (M17) over the northern Chihuahuan Desert (Figure 1). During the A13 event, dust from the southwest CP was transported to the San Juan Mountains in Colorado, which resulted in the second strongest dust loading of 4.58 gm^{-2} in the 2013 water year (October–September) measured at the Senator Beck Basin monitoring site (Skiles et al., 2015). A southwest–northeast oriented dust plume was present over the southwest CP on April 16th (Figure 1a). Around 1800 UTC on the 16th, the Meteorological Terminal Aviation Routine Weather Report (METAR) station at Cortez, Colorado (METAR, 2022), reported a visibility less than 10 km with a southwesterly wind speed of greater than 15 ms^{-1} (Figure S1 in Supporting Information S1). For two more hours, the southwesterly wind continued with a wind speed of $>10 \text{ ms}^{-1}$. Around 2000 UTC, visibility was reduced to $<2 \text{ km}$. Another METAR station at Durango, Colorado (METAR, 2022) also reported a reduction in visibility ($<10 \text{ km}$) with a southwesterly wind speed of $>10 \text{ m s}^{-1}$ around 1800 UTC.

In the M17 case, dust was primarily emitted from the northern Chihuahuan Desert, near the United States–Mexico border. A southwest–northeast-oriented, thick dust plume formed over El Paso, Texas (Figure 1b). The El Paso airport METAR station (METAR, 2022) reported visibility of $<10 \text{ km}$ $\sim 1800 \text{ UTC}$ on March 23 with a wind speed of 10 ms^{-1} (Figure S1 in Supporting Information S1). During 2000–2100 UTC, the visibility was reduced to $<2 \text{ km}$ with a west–southwesterly wind speed of $>15 \text{ ms}^{-1}$. Later, the dust plume widened and was advected poleward (<https://www.weather.gov/lub/events-2017-20170323-wind>).

3. Data and Methodology

3.1. Reanalysis Data Set

The fifth-generation European Center for Medium-Range Weather Forecasting, hourly, (0.25° horizontal pixel resolution) reanalysis data set ERA5 (Hersbach et al., 2020a, 2020b) was used to describe the large-scale meteorological features responsible for organization of the two dust events. ERA5 provides an hourly data set starting from 1979. We used charts of horizontal wind, and geopotential height at the 250 hPa and 600 hPa levels, to describe the upper- and mid-level dynamics. For near-surface meteorological interpretations, we used charts of mean sea level pressure (MSLP) and 10 m wind made from ERA5.

3.2. Model Description and Experimental Design

The WRF-Chem (version 4.2) (Grell et al., 2005) simulations were performed using a one-way nesting of three domains. The coarsest and outer domain has a horizontal of 18 km and subsequent additional nested domains have 6 and 2 km. The 18 km parent domain covered most of the Southwestern states (Figure 2). The atmosphere was divided into 41 vertical levels with the top of the atmosphere set at 50 hPa. The nested configuration used one-way forcing such that the inner domains did not feedback into their respective parent domains. The model was

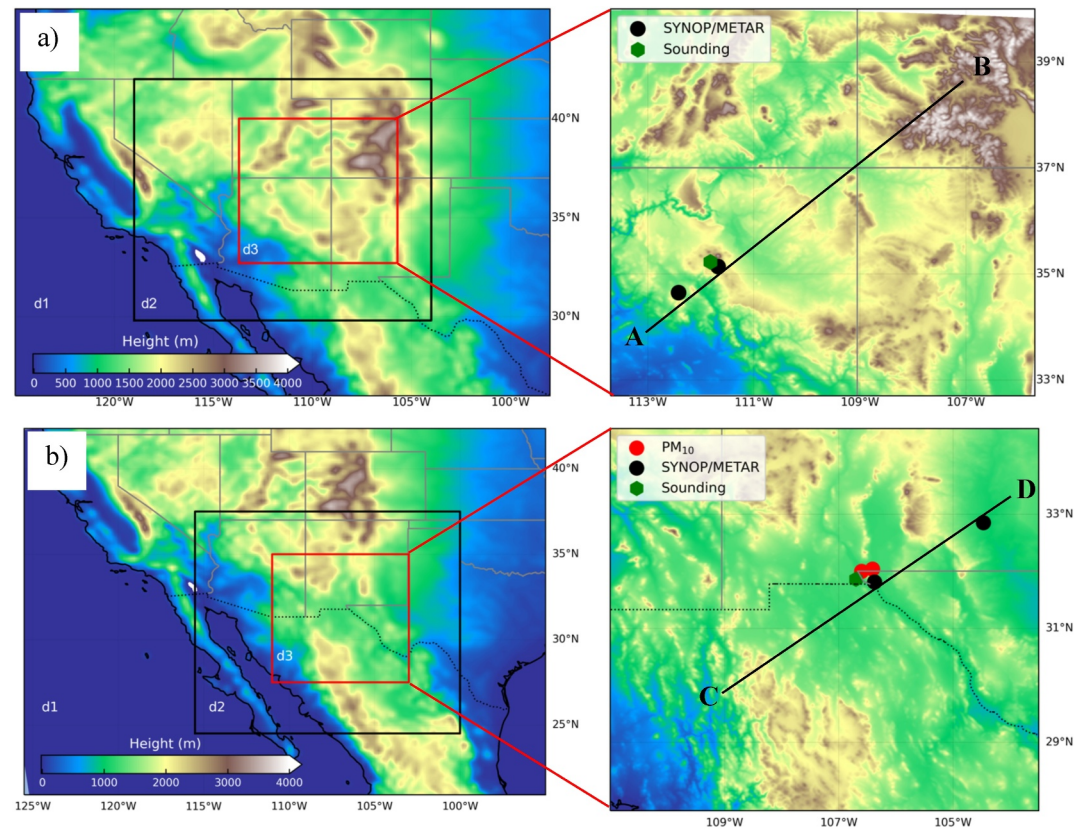


Figure 2. WRF-Chem simulation domains with available observational network for (a) A13 and (b) M17 dust events. The line AB (−113°W, 34°N to −107°W, 38.5°N) in Figure 1a and CD (−109°W, 30°N to −104.5°W, 33.5°N) in Figure 1b are for vertical cross-section analysis for the A13 and M17 cases, respectively.

initialized using the ERA5 reanalysis data set, and the lateral boundaries of the parent domain were updated hourly. Both simulations were run for 42 hr. The A13 simulation started at 1200 UTC on 15 April 2013, and ended at 0600 UTC on 17 April 2013, while the M17 simulation started at 1200 UTC on 22 March 2017, and ended at 0600 UTC on 24 March 2017. The 2 km nested variables were saved every 30 min and used for all analyses presented here.

3.2.1. Model Physics and Chemistry Parameterizations

The physics and chemistry parameterizations used in our simulations are summarized in Table 1. The cumulus parameterization was used only on the 18 km domain and follows the new Grell scheme (Grell & Dévényi, 2002). The inner nested domains (6 and 2 km) allowed convection to develop explicitly. All other physics and chemistry schemes used are identical across each domain. More details on the physical parameterizations can be found at https://www2.mmm.ucar.edu/wrf/users/physics/phys_references.html.

The chemistry option included was the GOCART aerosol module without ozone chemistry (Ginoux et al., 2001). The dust emission scheme followed the AFWA dust emission scheme (LeGrand et al., 2019) with the CW16 MODIS albedo-based drag partition which describes the aerodynamic roughness changing over space (500 m pixels) and over time (daily). A summary of the implementation of the CW16 drag partition in the AFWA dust emission scheme is presented in Section 3.2.2.

To compare the simulated dust evolution with the observation, we used simulated aerosol optical depth (AOD) at 550 nm and PM_{10} . We calculated AOD by vertically integrating extinction coefficients for the whole atmospheric column (see appendix C in Ukhov et al., 2021). PM_{10} is calculated using the following equation:

$$PM_{10} = \rho \cdot (Dust_1 + Dust_2 + Dust_3 + Dust_4 \cdot d_{10} + SEAS_1 + SEAS_2 + SEAS_3) \quad (1)$$

Table 1
Physics and Chemistry Schemes Used in the WRF-Chem Model

WRF-Chem	v4.2 (Grell et al., 2005)		
Simulation domains	3		
Horizontal resolutions	18 km, 6 km, and 2 km		
Vertical levels	41		
Initial and boundary conditions	ERA5 (Hersbach et al., 2020a, 2020b)		
Parameterizations	Scheme	Namelist variable	Option
Physics			
Microphysics	Thompson (Thompson et al., 2008)	mp_physics	8
Radiation (long and shortwave)	RRTMG (Iacono et al., 2008)	ra_lw(sw)_physics	4
Surface model	Noah (Ek et al., 2003)	sf_surface_physics	2
Surface layer	MYNN (Nakanishi & Niino, 2004a, 2004b)	sf_sfclay_physics	5
Planetary boundary layer	MYNN2.5 level (Nakanishi & Niino, 2004a, 2004b)	bl_pbl_physics	5
Cumulus parameterization (D01 only)	Grell 3D (Grell & Dévényi, 2002)	cu_physics	5
Chemistry			
Chemistry	GOCART simple/no ozone chemistry	chem_opt	300
Dust emission	AFWA (LeGrand et al., 2019)	dust_opt	3
Aerosol Radiative feedbacks	Off	aer_ra_feedback	0
Aerosol optics	Maxwell approximation (Bohren & Huffman, 2007)	aer_op_opt	2

Where ρ is dry air density (kgm^{-3}), d_{10} ($=0.373$) is the mapping coefficient, and DUST_{1-4} and SEAS_{1-3} are mixing ratios (μgkg^{-1}) of the dust in the first four bins and sea-salt in the first three bins, respectively.

3.2.2. Implementation of Drag Partition in AFWA

The AFWA dust emission module, as implemented in WRF-Chem, does not represent dynamic roughness effects on dust emission. Instead, the default AFWA scheme incorporates a static mask designed to block dust emission from vegetated areas derived from a relatively coarse, 1-degree resolution land cover data set and further restricts dust emission from areas where the aerodynamic roughness length is >20 cm (LeGrand et al., 2019). This setting essentially limits dust emission in the AFWA scheme to areas classified by the model as barren, cropland, savanna, grassland, or shrubland.

For this study, we used a version of AFWA dust emission module configured with the CW16 drag partition described by LeGrand et al. (2023). Specifically, we used the ALT3 configuration of LeGrand et al. (2023), which removes all forms of vegetation masking built into the dust emission code. The ALT3 configuration also eliminates the influence of a dust source strength parameter that functions as a spatially varying available sediment supply tuning factor. Removing this source strength parameter effectively causes the emission scheme to assume that all areas are equally erodible.

In the base version of the AFWA dust scheme, saltation flux $Q(D_{s,p})$ ($\text{gcm}^{-1}\text{s}^{-1}$) is calculated following:

$$Q(D_{s,p}) = \begin{cases} C \frac{\rho_a}{g} u_*^3 \left(1 - \frac{u_{*ts}(D_{s,p}, \theta)^2}{u_*^2}\right) \left(1 + \frac{u_{*ts}(D_{s,p}, \theta)}{u_*}\right), & u_* > u_{*ts}(D_{s,p}, \theta) \\ 0, & u_* \leq u_{*ts}(D_{s,p}, \theta), \end{cases} \quad (2)$$

where $C = 1$ is a proportionality constant, ρ_a is air density at the lowest model level (g cm^{-3}), g is the acceleration due to gravity (cm s^{-2}), u_* is total wind friction velocity (or shear velocity) (cm s^{-1}), $u_{*ts}(D_{s,p}, \theta) = u_{*ts}(D_{s,p}) * f(\theta)$

is moisture-corrected entrainment threshold friction velocity (cm s^{-1}), $D_{s,p}$ is effective diameter (μm) and $f(\theta)$ is the soil moisture correction function (Fécan et al., 1999). The entrainment threshold is fixed over space to soil classes and varies over time only as a function of soil moisture. The approach is momentum limited that is, when there is sufficient momentum to exceed the threshold there is transport of sediment. Like other dust models, this approach assumes that there is an infinite supply of dry, loose erodible material available for transport given sufficient momentum. Following drag partition theory, the total wind shear velocity (u_*) is divided into wind shear velocity acting on roughness elements such as vegetation and rocks (u_{r*}) and the exposed soil surface (u_{s*}) following:

$$u_* = u_{r*} + u_{s*} \quad (3)$$

Since dust mobilization at the soil surface depends on u_{s*} rather than u_* (Chappell & Webb, 2016; Webb et al., 2020), the saltation flux $Q(D_{s,p})$ depends on u_{s*} and its corresponding entrainment threshold (u_{*ts}) value:

$$Q(D_{s,p}) = \begin{cases} C \frac{\rho_a}{g} u_{s*}^3 \left(1 - \frac{u_{*ts}(D_{s,p}, \theta)^2}{u_{s*}^2}\right) \left(1 + \frac{u_{*ts}(D_{s,p}, \theta)}{u_{s*}}\right), & u_{s*} > u_{*ts}(D_{s,p}, \theta) \\ 0, & u_{s*} \leq u_{*ts}(D_{s,p}, \theta) \end{cases} \quad (4)$$

The CW16 provides a method to directly parameterize u_{s*} based on the MODIS daily albedo product (Collection 6, MCD43A1; Schaaf & Wang, 2021). With this product, we calculated $\frac{u_{s*}}{U_h}$ following:

$$\frac{u_{s*}}{U_h} = 0.0311 \left(e^{-\frac{w_{ns} 1.131}{0.016}} \right) + 0.007, \quad (5)$$

where w_{ns} was obtained from MODIS based on sheltering being equivalent to shadow (Raupach & Lu, 2004) cast by roughness following Chappell and Webb (2016), Chappell et al. (2018) and LeGrand et al. (2023), and U_h is the wind velocity at a given height (h) (ms^{-1})—used here at 10 m height above ground level (U_{10}). Finally, the friction velocity at the soil surface (u_{s*}) was obtained by multiplying u_{s*}/U_h by 10 m wind speed as in Equation 5.

$$u_{s*} = U_{10m} * \left(\frac{u_{s*}}{U_h} \right) \quad (6)$$

Where U_{10m} is the 10 m wind speed. Detailed descriptions of the MODIS albedo-based drag partition approach (Chappell et al., 2018; Chappell & Webb, 2016) and its implementation in the AFWA dust emission scheme are provided in Michaels et al. (2022).

3.3. Observational Data Sets

To describe the evolution of the dust events and evaluate the WRF-Chem simulations, we used wind and visibility data sets from different METAR stations (METAR, 2022) distributed across the study area (Figure 2). Additionally, we used radiosonde data (Sounding, 2022) collected at 12-hr intervals from the weather balloons released at Flagstaff, Arizona, and Santa Teresa, New Mexico stations to evaluate model performance throughout the atmospheric column. To describe the dust evolution and model-dependent variable accuracy, we also used PM_{10} concentration and AOD data from surface observations and satellite retrievals at 10 km spatial resolution. The AOD data were obtained from MODIS at 550 nm (combined Dark Target and Deep Blue algorithm) (MODIS, 2022). The PM_{10} hourly data were obtained from the US Environmental Protection Agency (EPA) (PM10, 2022). To describe the dust source areas within the WRF-Chem model, we assessed the vegetation conditions using plant functional group annual fractional cover estimated by the Rangeland Analysis Platform (RAP) including cover of annual forbs and grasses (AFG), perennial forbs and grasses (PFG), and shrubs (SHR) (Jones et al., 2018). As the RAP plant functional group cover estimates are modeled using historical Landsat satellite, gridded meteorological data and field data collected across the western US throughout the summer growing season, we used estimates from the years preceding the case study dust events (which occurred in spring 2013 and 2017) as those data would provide better indicators of ground cover than estimates produced from field measurements collected in the same year but following the dust events.

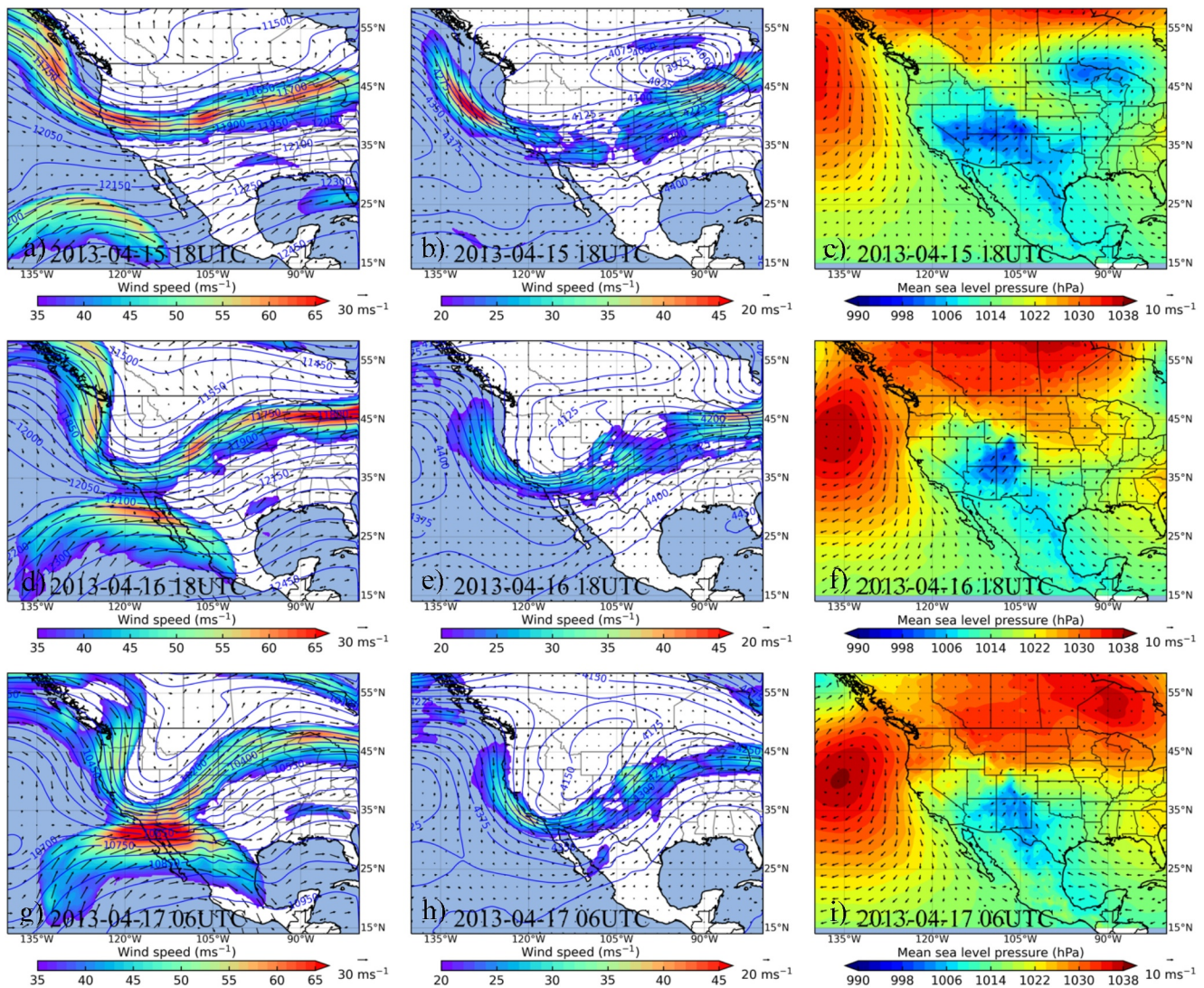


Figure 3. 36-hr evolution of (left column) 250 hPa horizontal wind isotachs (ms^{-1}) and geopotential height (m), (middle column) 600 hPa horizontal wind isotachs (ms^{-1}) and geopotential height (m), and (right column) 10 m wind barbs (ms^{-1}), and mean sea level pressure (hPa) for the A13 dust events. Meteorological fields are from ERA5.

4. Results

4.1. Large-Scale Meteorological Conditions for Organization of the Dust Events

The large-scale meteorological description of these dust events is focused on the evolution of the Polar jet stream (PJ) and Sub-tropical jet stream (STJ), mid-tropospheric and low-level flow as both dust events were linked baroclinic mid-latitude cyclones. Figures 3 and 4 show the evolution of the 250 hPa (hereafter upper-level) and 600 hPa (hereafter mid-level) horizontal winds and geopotential height, MSLP, and 10 m wind for the A13 and M17 dust events, respectively.

In the A13 dust events, at 1800 UTC on the 15th, the PJ streak core was located over the Sierra Nevada Mountains and the STJ streak core was located over the subtropical Eastern Pacific (Figure 3a). The mid-level flow over the CP was weak (Figure 3b). As time progressed, the PJ and STJ streaks started to merge (Figure S2 in Supporting Information S1) and completed their merger at 1800 UTC on the 16th (Figure 3d). While merging, the PJ propagated toward the equator and the upper-level trough was located over southern California, while the STJ streak core propagated northeastward and was located over Baja California. When the PJ and STJ merged, strong mid-level southwesterly winds developed over the southwestern CP (northeastern Arizona), where dust was

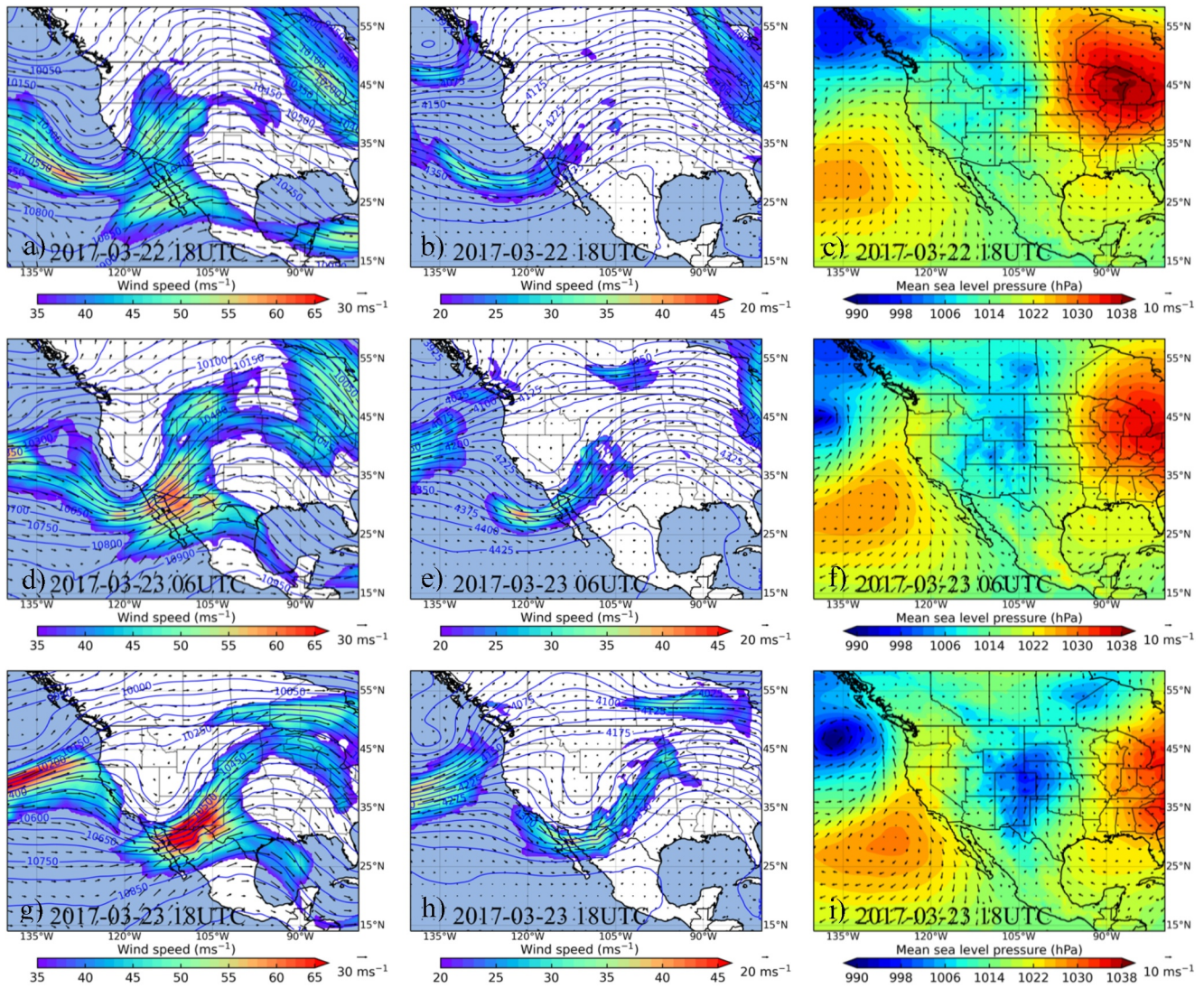


Figure 4. 24-hr evolution of (left column) 250 hPa horizontal wind isotachs (ms^{-1}) and geopotential height (m), (middle column) 600 hPa horizontal wind isotachs (ms^{-1}) and geopotential height (m), and (right column) 10 m wind barbs (ms^{-1}) and mean sea level pressure (hPa) for the M17 dust events. Meteorological fields are from ERA5.

emitted (Figure 3e). For the next 12 hr, the unified PJ and STJ resulted in a strong jet streak over Mexico, southern California, and southern Arizona (Figure 3g). The intensification of the unified jet streak represents the culmination of an acceleration process evident earlier in the STJ streak. The mid-level southwesterly wind over the lower CP also intensified just below the left exit region of the unified jet streak core (Figure 3h). Additionally, a uniform, strong, southwesterly, mid-level sub-synoptic jet or “jetlet” extends from southwest Arizona to the CP.

At the surface, at 1800 UTC on the 15th, a surface cyclone was located over the CP and Great Basin with relatively strong southwesterly 10 m winds over Arizona and New Mexico compared to their surrounding (Figure 3c). Twenty-four hours later, at 1800 UTC on the 16th, when the PJ and STJ streaks unified, the cyclone center was located over the CP (Figure 3f). At this time, jet streak merging, surface minimum pressure over the CP, and mid-level wind maxima just over the CP occurred concurrently (Figures 3d–3f). The strong southwesterly near-surface wind caused by the strong pressure gradient between the intensifying surface cyclone over the CP and its upstream region lifted dust from the southwestern CP (Figures 3c and 3f and Figure S3 in Supporting Information S1). As the low-pressure system weakened and moved east, the near-surface southwesterly flow weakened, and dust emission ceased. However, strong mid-level flow persisted over the CP, enabling lofted dust to be transported to the San Juan Mountains.

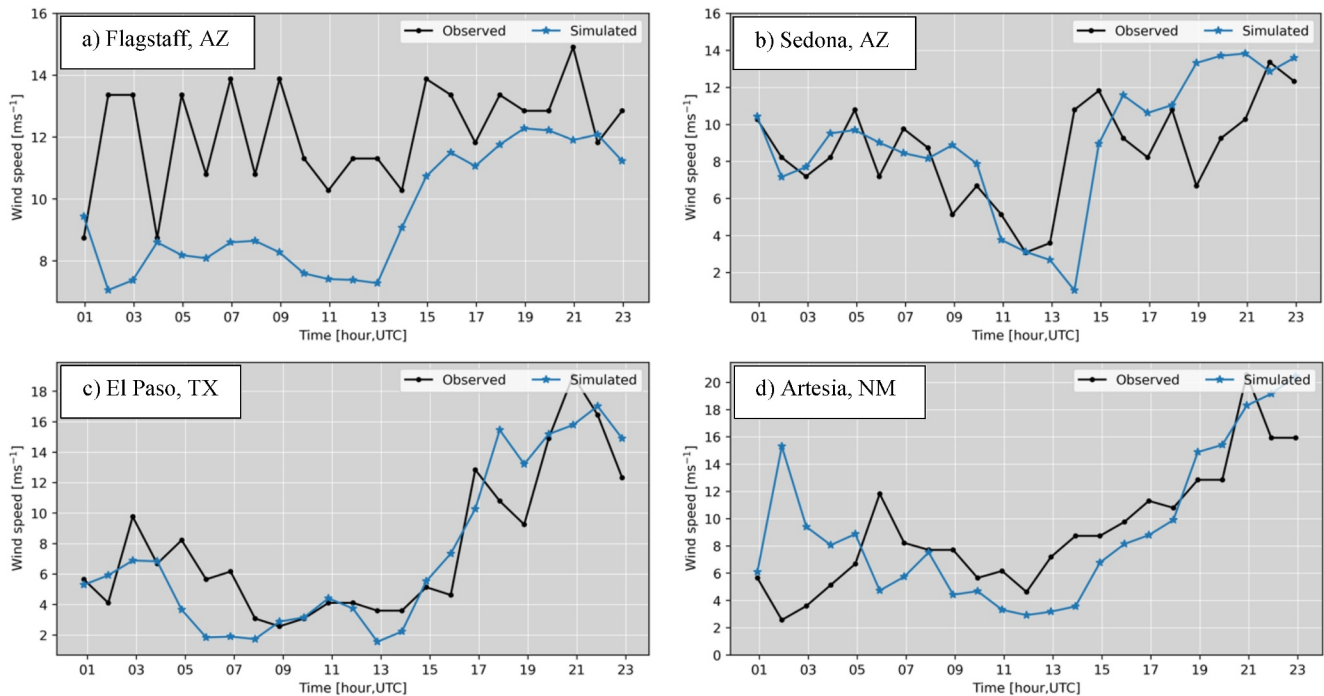


Figure 5. Observed and WRF-Chem simulated 10 m height wind speed at (a) Flagstaff and (b) Sedona in Arizona for 16 April 2013, and at the (c) El Paso Airport in Texas and (d) Artesia in New Mexico for 23 March 2017.

In the M17 case, at 1800 UTC on the 22nd the PJ and STJ streaks started to merge over Baja California (Figure 4a). This merger is similar to the merger seen in the A13 case. However, in contrast to the A13 event, the mid-level wind over the CP was relatively weak at the time of the jet merger (Figure 4b). Twelve hours later, at 0600 UTC on the 23rd, as the PJ and STJ streaks continued to merge, a strong jet core developed over Baja California and the United States-Mexico border (Figure 4d). With this merger, southwesterly mid-level flow intensified over the CP and upstream over southwestern Arizona (Figure 4e). After 12 hr, at 1800 UTC on the 23rd, the unified jet core intensified further and was located over the northern Chihuahuan Desert (Figure 4g). The mid-level wind intensified in a similar manner and was located just below the exit region on the poleward side of the unified jet core (Figure 4h). A southwesterly-northeasterly oriented elongated band of mid-level winds formed over the northern Chihuahuan Desert.

At the surface, at 1800 UTC on the 22nd, that is, when the PJ and STJ streaks started to merge, relatively high pressure was resided over the New Mexico and its surrounding (Figure 4c). Over the northern Chihuahuan Desert, the near-surface wind was weak (Figure 4c). Twelve hours later, at 0600 UTC on the 23rd, when the PJ and STJ streaks merged and a unified jet streak formed, the low-pressure system started to move further equatorward over Colorado and northern New Mexico (Figure 4f). After 12 hr, at 1800 UTC on the 23rd, that is, when the unified jet intensified over the northern Chihuahuan Desert, the surface pressure deepened over Colorado and New Mexico (Figure 4i). Strong southwesterly-southerly near-surface flow developed due to the strong northeastward pressure gradient between Colorado and New Mexico and its upstream region over the Chihuahuan Desert (Figure 4i), which lifted dust from the northern Chihuahuan Desert. The mid-level wind maxima over the northern Chihuahuan Desert resulted in the transport of entrained dust toward the Colorado Rocky Mountains under the influence of lower-to-mid level cyclonic flow (Figures 4h and 4i).

4.2. WRF-Chem Simulations and Evaluation

4.2.1. Model Evaluation for Dust Emission and Transport

To evaluate the model performance, we compare observed and simulated wind patterns that drive dust emission and subsequent transport. The comparison between simulated and observed 10 m wind at the Flagstaff METAR station, for the A13 episode, showed that the model underestimated the wind speed between 0100 and 1300 UTC

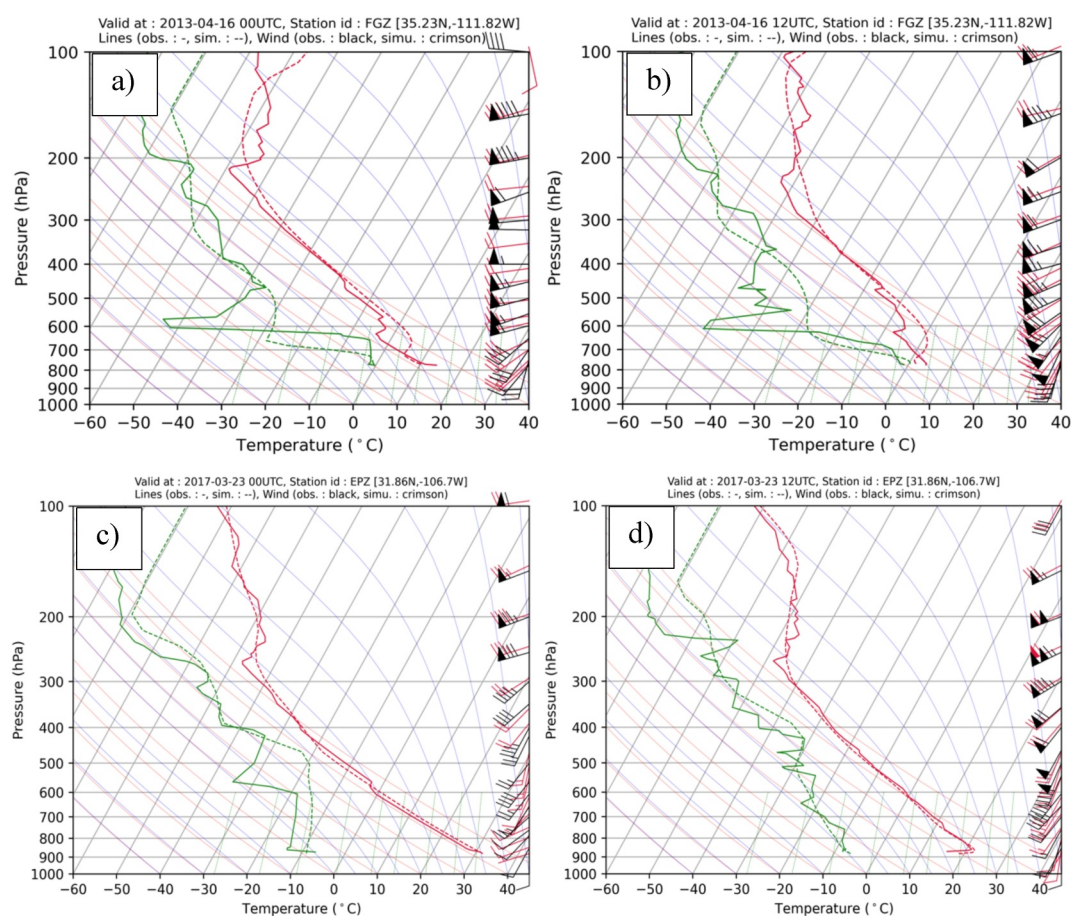


Figure 6. SkewT-LogP diagram at Flagstaff, Arizona (KFGZ) for (a) 0000 UTC and (b) 1200 UTC 16 April 2013, and at Santa Teresa, New Mexico (KEPZ) valid for (c) 0000 UTC and (d) 1200 UTC 23 March 2017.

on the 16th (Figure 5a). Simulated winds ranged between 7 and 9 ms^{-1} , while observed winds ranged between 9 and 13 ms^{-1} . These discrepancies in wind patterns are probably because Flagstaff METAR station is situated in the valley region and the model did not capture the small-scale flow interaction in a complex terrain. Additionally, inaccurate representation of land use classification could be another factor for large discrepancy in high-elevation mountains in the Southwest (Gallagher et al., 2022). However, starting at 1400 UTC, observed and simulated wind speeds show a close correspondence. Between 1500 and 2300 UTC, observed wind speed ranged between 10 and 15 ms^{-1} , while simulated wind speed ranged between 11 and 12 ms^{-1} . A closer correspondence between observed and simulated wind speed is seen at the Sedona METAR station, where wind speed decreased during 0000–1200 UTC on the 16th (Figure 5b). Starting at 1300 UTC, when southwesterly winds arrived at this location, both simulated and observed wind speed started to increase.

Wind comparison at the El Paso Airport METAR station for the M17 episode, shows that the observed 10 m wind on the 23rd decreased from 10 ms^{-1} at 0300 UTC to 3 ms^{-1} at 0900 UTC (Figure 5c). Beginning at 1000 UTC, wind speed started to increase and reached its peak value of >18 ms^{-1} at 2200 UTC. The simulated wind speed also followed a similar pattern. At the Artesia, METAR station, before 1200 UTC on the 23rd, wind speed remained mostly below 8 ms^{-1} except at 0600 UTC (12 ms^{-1}) (Figure 5d). Beginning at 1300 UTC, wind speed started to increase and reached its peak value of 20 ms^{-1} at 2100 UTC. The simulation also produced a similar pattern of 10 m wind at this location with very close correspondence during 1500–2300 UTC.

A sounding comparison at Flagstaff (KFGZ), for the A13 episode, shows intensified lower-mid tropospheric southwesterly winds at 1200 UTC compared to 0000 UTC on the 16th, suggesting strong southwesterly winds were responsible for dust lofting (Figures 6a and 6b). There was a strong increase in observed wind speed below 700 hPa. Compared to observation, the model underestimated the vertical profiles of wind at this station.

Nevertheless, both observed and simulated winds show an increase in the southwesterly component at 1200 UTC compared to 0000 UTC. Additionally, temperatures below 700 hPa are in close agreement during these 12-hr. However, the model overestimated air temperature near the 600–700 hPa layer. Above 600 hPa, again both temperatures are in close agreement.

The Santa Teresa (KEPZ) simulated sounding, for the M17 dust events, shows close correspondence with the observed sounding (Figures 6c and 6d). Two notable features can be seen at 1200 UTC when compared to 0000 UTC: (a) intensification of the low-level southwesterly winds and development of the mid-level strong winds between 700 and 500 hPa, and (b) a deep dry adiabatic layer, suggesting a deep mixed layer. This deep mixed layer favors the mixing of lifted dust, and the strong mid-level southwesterly wind helps with the northeastward transport of dust. The above comparison with available observational data sets shows that the WRF-Chem model reproduced the general pattern of the observed meteorology in these two cases. Next, we evaluate dust evolution for the two events.

4.2.2. Dust Source Regions and Dust Loading Over the Colorado Plateau

In the A13 dust event, the southwest CP (mostly northeast Arizona) and northwest New Mexico were the major dust source regions (Figure 7). The simulations show dust emitting from different source regions across the southwestern CP. At 1200 UTC on the 16th, dust emission started with the arrival of southwesterly strong near-surface flow (Figure 7a). At that time, a band of dust emission flux was present northeast of Flagstaff, Arizona and contributed to the evolution of the first dust plume as revealed in the simulated dust load (Figure 7b). Two hours later at 1400 UTC, the dust emitting region expanded, dust emission flux intensified, and dust loading increased (Figures 7c and 7d). This resulted in a strong simulated northeast-traveling dust plume consistent with northeast-traveling observed dust plume (Figures 1d and 7c and 7d).

At 1400 UTC on the 16th, dust emission flux started to increase in Farmington, New Mexico resulting in a second dust plume (Figures 7a–7d). After 1400 UTC, dust emission flux further increased in the northeastern corner of Arizona and northwestern corner of the New Mexico, which resulted in two strong dust plumes consistent with observed dust plumes seen in the satellite imagery (Figures 1a and 1b and 7e and 7f). Both the dust plumes ultimately advected in a northeast direction toward the San Juan Mountains.

4.2.3. Spatiotemporal and Vertical Evolution of Dust Over the Colorado Plateau

Figure 8 shows AOD simulated at 2 km resolution and observed at 10 km resolution to compare the spatial evolution of dust plumes. Simulated AOD mostly comes from dust and observed AOD was attributed to dust in the absence of wildfire. At 1800 UTC on the 16th, the simulated dust plumes were present over the Four Corners region (AZ, UT, CO, and NM) (Figure 8a). Dust Plume 1 was present over the northeast corner of Arizona and extended to the Four Corners region and Dust Plume 2 was present over northwestern New Mexico in San Juan County. The closest MODIS-Terra overpass at 1810 UTC shows the coherent patterns of the dust plumes (Figure 8b). The peak AOD value of the observed and simulated Dust Plume 1 was ~ 0.9 . For Dust Plume 2, the peak observed AOD value was ~ 0.9 , while the simulated AOD was ~ 0.6 , which suggests that the model underestimated AOD in Dust Plume 2. Nevertheless, the spatial distribution of the simulated dust plumes closely matches the observed dust plumes (Figure 8, and Figure S4 in Supporting Information S1).

Figure 9 shows the vertical cross-sections of hourly simulated dust concentration and potential temperature along the line AB (see Figure 2) for 1200–1900 UTC on the 16th. We focused on the vertical distribution of dust since this is critical to long-range transport from the desert southwest into the San Juan Mountains. At 1200 UTC (local time 6 a.m.), the small dust emission flux just northeast of Flagstaff resulted in low magnitude near-surface dust concentration (Figure 9a). The stable PBL, as revealed by the low-level vertically compressed isentropes, did not allow the mixing of lifted dust to greater heights. Between 1300 and 1400 UTC, lofted dust remained near the surface in the stable PBL (Figures 9b and 9c). At 1500 UTC (local time 9 a.m.), the near-surface dust concentration started to increase due to intensifying southwesterly winds (Figure 9d). After sunrise, the PBL grew in response to diurnal heating at the surface which resulted in strong vertical mixing within the PBL and dust expansion to greater heights. Between 1600 and 1700 UTC, the dust layer advected northeastward and extended above 2 km in height between 35.5 and 38°N with a dust concentration of $\sim 1500 \mu\text{g kg}^{-1}$ (Figures 9e and 9f). The vertical expansion of the dust plume further increased between 1800 and 1900 UTC due to increasing dust emission flux and strong mixing in the deep PBL (Figures 7g and 9g and 9h). Around 1900 UTC, the dust layer was further advected poleward and made first contact with the San Juan Mountains, which is supported by the decrease in visibility at Cortez and Durango

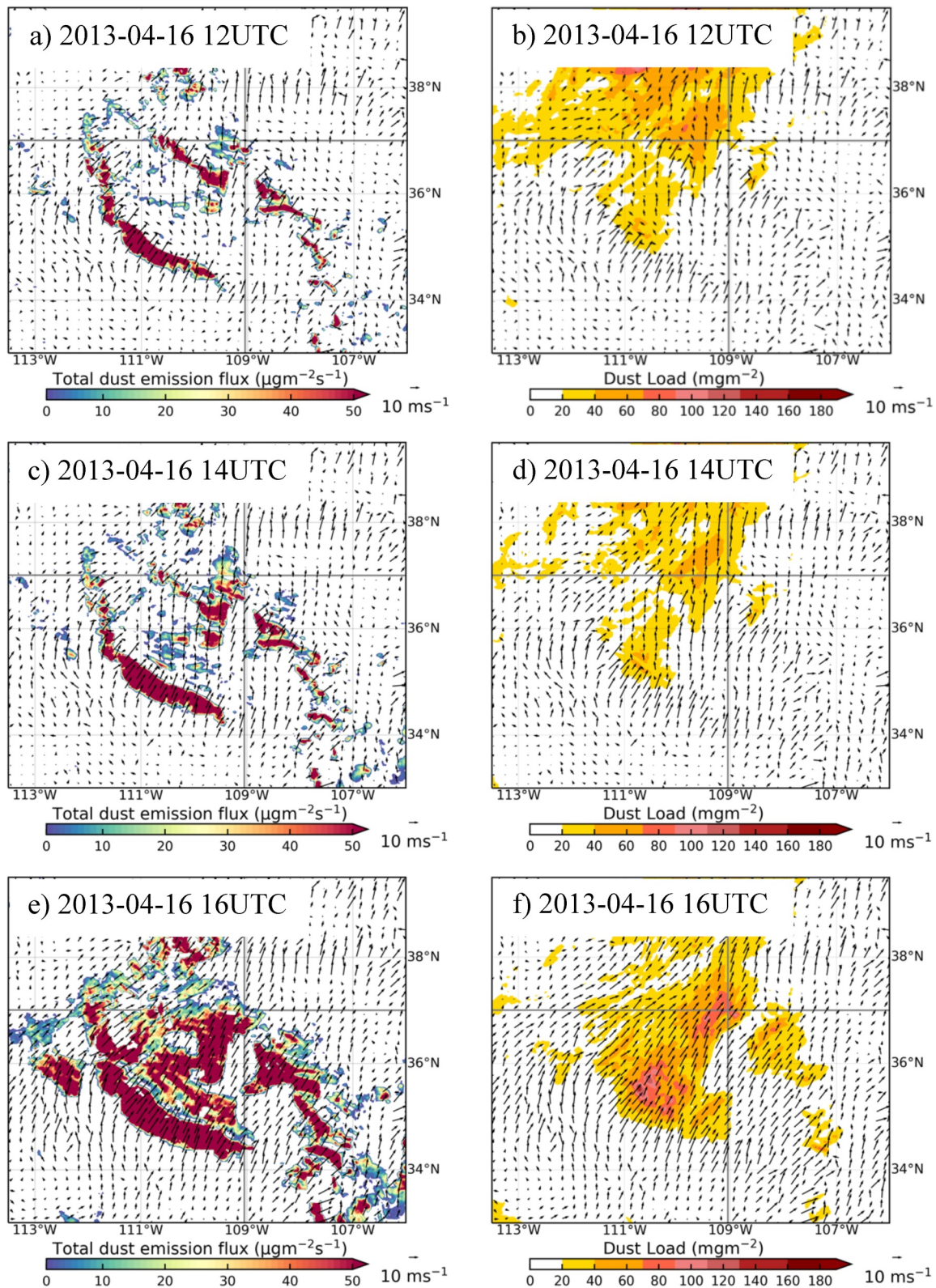


Figure 7. WRF-Chem simulated (a, c, e) 10 m wind and dust emission flux and (b, d, f) 10 m wind and dust load at (a, b) 1200, (c, d) 1400, and (e, f) 1600 UTC 16 April 2013 over the Colorado Plateau.

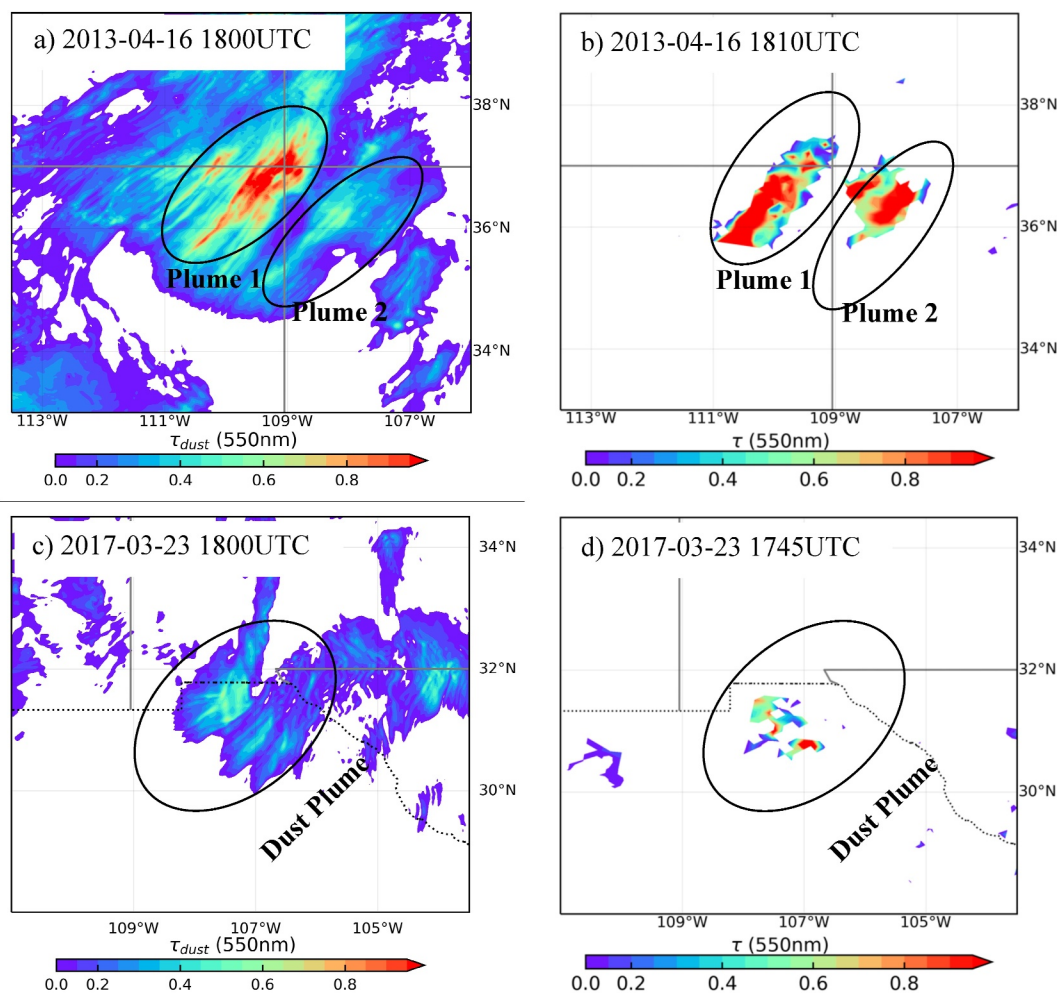


Figure 8. Comparison of aerosol optical depth, (left) WRF-Chem simulated at 2 km grid resolution and (right) MODIS-Terra at 10 km spatial resolution for (top panel) A13 and (bottom panel) M17 dust events.

METAR stations with strong southwesterly winds (Figure 9h and Figure S1 in Supporting Information S1). The northeastward advection of the dust plumes to the San Juan Mountains was due to the strong mid-level southwesterly flow that developed over the CP region (discussed earlier in Section 4.1).

4.2.4. Dust Source Regions and Dust Loading Over the Chihuahuan Desert

The northern Chihuahuan Desert was the major dust source in the M17 dust event. Around 1400 UTC on the 23rd, the southwesterly flow over the northern Chihuahuan Desert was weak with little dust emission and no significant dust loading in the atmosphere (Figures 10a and 10b). Two hours later at 1600 UTC, the southwesterly flow intensified, which resulted in increased dust emission flux and dust loading across many parts of the northern Chihuahuan Desert near the United States-Mexico border (Figure 10c). Between 1600 and 1800 UTC, the southwesterly flow further intensified and resulted in more dust emissions from the northern Chihuahuan Desert (near northern Mexico, southern New Mexico, and western Texas). The intensified dust emission flux subsequently increased dust loading resulting in a northeastward-traveling strong dust plume consistent with the observed dust plume (Figures 1b and 10e–10h).

4.2.5. Spatiotemporal and Vertical Evolution of Dust Over the Chihuahuan Desert

We used the simulated and observed AOD to describe the spatial evolution of the dust. At 1800 UTC on the 23rd, the simulation showed a thick dust plume over the northern Chihuahuan Desert (Figure 8c), near the United States-Mexico border. The closest MODIS-Terra overpass at 1745 UTC on the 23rd showed a similar pattern of

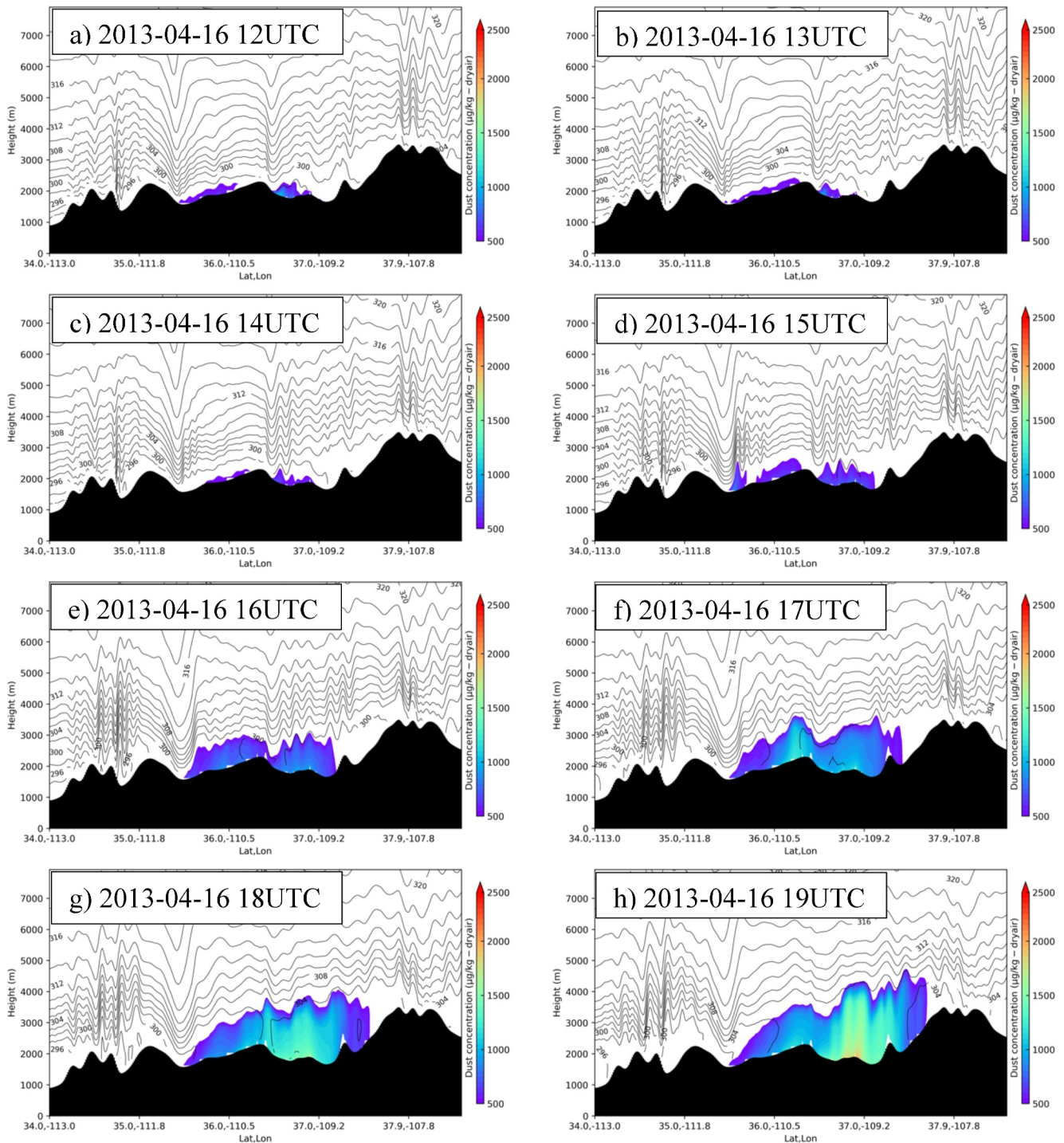


Figure 9. WRF-Chem simulated vertical cross-sections of potential temperature (K) and dust concentration along AB (see Figure 1) at (a) 1200, (b) 1300, (c) 1400, (d) 1500, (e) 1600, (f) 1700, (g) 1800, and (h) 1900 UTC 16 April 2013.

the dust plume (Figure 8d). The peak value of the observed AOD was ~ 0.6 – 0.8 , while the simulated peak value was ~ 0.6 , suggesting an underestimation of simulated AOD. Nonetheless, the spatial pattern of the observed dust plume was captured by the simulation (Figure 8d and Figure S4 in Supporting Information S1).

To describe the vertical evolution of the dust, we used the vertical cross-section of simulated dust and potential temperature along the line CD (see Figure 2). At 1700 UTC on the 23rd, dust emission flux over the northern

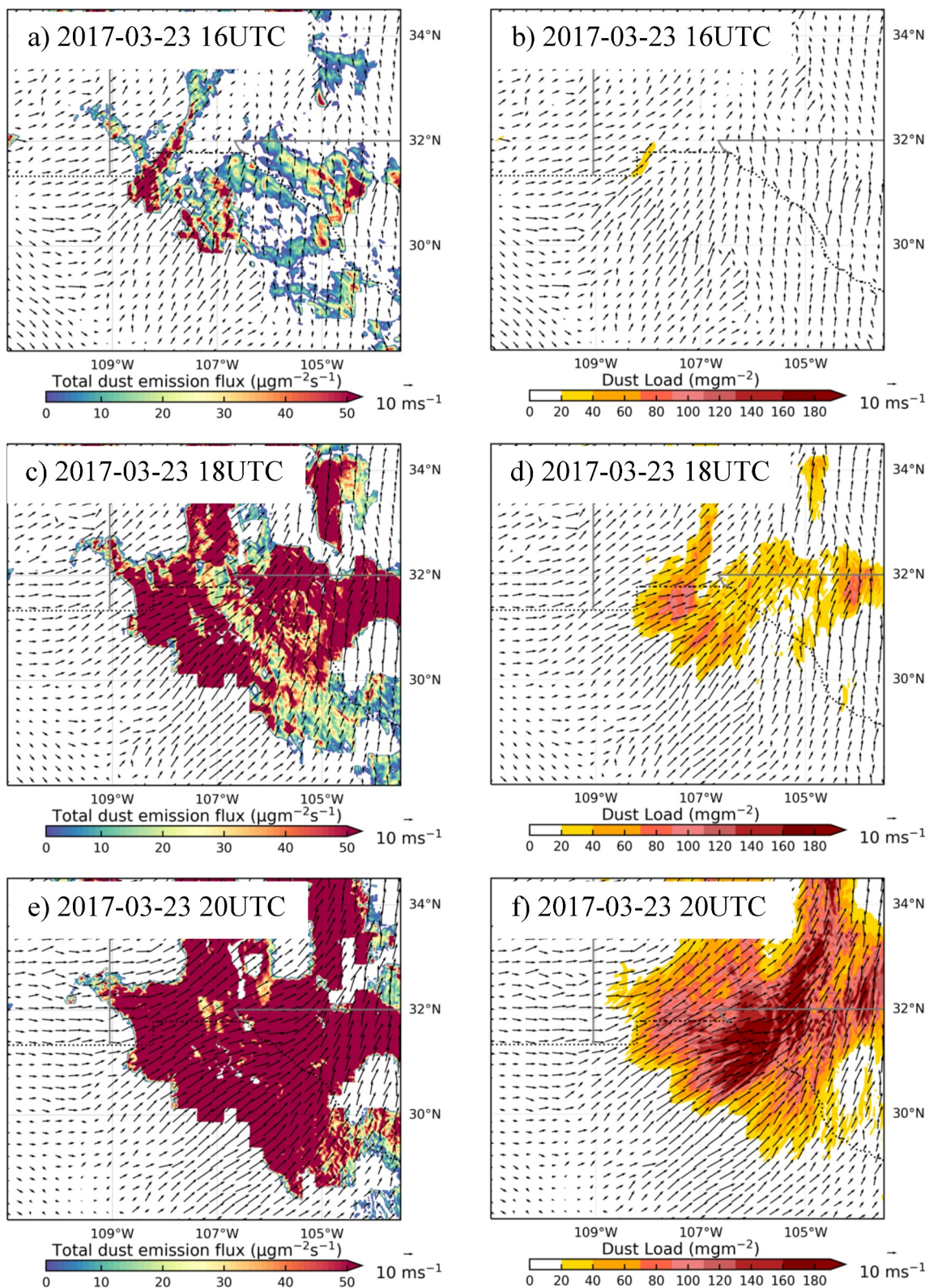


Figure 10. WRF-Chem simulated (a, c, e) 10 m wind and dust emission flux and (b, d, f) 10 m wind and dust load at (a, b) 1400, (c, d) 1600, and (e, f) 1800 UTC 23 March 2017.

Chihuahuan Desert was small, and a significant amount of dust was not present in a well-mixed layer (Figure 1a). One hour later at 1800 UTC, dust emission flux increased and resulted in a thick dust plume with a dust concentration of $\sim 700 \mu\text{g kg}^{-1}$ over the northern Chihuahuan Desert (Figure 11b). At 1900 UTC, the dust plume expanded horizontally and vertically in a growing daytime PBL and reached the El Paso, Texas region (Figure 11c). At 2000 UTC, while propagating northeastward, the dust plume expanded vertically reaching above 2.5 km due to strong vertical mixing (Figure 11d). Between 2000 and 2200 UTC, a strong dust plume impacted the El Paso region, which is supported by the decrease in visibility at the El Paso METAR station (Figures 11d–11f and Figure S1 in Supporting Information S1). Ultimately, the available dust plume was transported north-eastward under the influence of strong mid-level southwesterly wind present over the northern Chihuahuan Desert/El Paso region (Figures 6c and 6d and Figure S5 in Supporting Information S1).

4.2.6. PM_{10} Evolution Over the Chihuahuan Desert

We further evaluated simulated dust evolution by comparing hourly PM_{10} at two air quality stations in southern New Mexico (Figure 2b). At the West Mesa station, before the arrival of the dust event, PM_{10} concentration remained very low during 0000–1800 UTC on the 23rd (Figure 12a). At 1900 UTC, PM_{10} concentration jumped to $>200 \mu\text{g m}^{-3}$, reached its maximum value of $\sim 1300 \mu\text{g m}^{-3}$ at 2100 UTC, and started to decrease but the concentration remained between 300 and $600 \mu\text{g m}^{-3}$ between 2200 and 2300. During 1900–2300 UTC, the simulated PM_{10} remained between 450 and $850 \mu\text{g m}^{-3}$. The model showed some discrepancies with observed PM_{10} at different times during the dust event but followed a similar pattern to the observed PM_{10} .

A similar PM_{10} pattern was observed at the Anthony station, where observed PM_{10} started to increase at 1800 UTC on the 23rd, reached its maximum value of $>2,400 \mu\text{g m}^{-3}$ at 2100 UTC, and then decreased to $600 \mu\text{g m}^{-3}$ at 2300 UTC (Figure 12b). The simulated PM_{10} started to increase at 1700 UTC, reached its maximum value of $\sim 1,600 \mu\text{g m}^{-3}$ at 2200 UTC, and then decreased to $\sim 1,100 \mu\text{g m}^{-3}$ at 2300 UTC. Again, we found some differences in observed and simulated PM_{10} during this dust event; however, both simulated and observed trends follow a similar pattern.

4.3. Analysis of Ground Cover Indicators in Modeled Dust Source Areas

Finally, we investigated and evaluated the dust sources in our WRF-Chem simulations. In the A13 case, the southwestern CP (northeastern Arizona) and Farmington, New Mexico, were the major sources that contributed to the two dust plumes. Large values of simulated dust emission fluxes were collocated with small annual fractional cover of annual forbs and grasses (AFG), PFG, and shrubs (SHR) in the preceding year (i.e., 2012). This outcome is supportive of the drag partition correction enabling dust emission from areas with overall less vegetation (Figures 13a–13c). The high dust-emitting regions in the southwest CP near the Little CRB seen in the simulation are recognized as having elevated susceptibility to dust emission on the CP (Li et al., 2013; Nauman et al., 2023).

In the M17 case, the primary modeled dust source region was the northern Chihuahuan Desert where vegetation cover was also very small (Figures 13c and 13d). Large dust emission fluxes were collocated with 2016 small annual fractional cover of AFG, PFG, and SHR. Although vegetation fractional cover data sets from the RAP are not available for the Mexican parts of the Chihuahuan Desert to compare dust emission fluxes and dust sources, these regions are recognized major sources of dust where wind can easily pick up dust due to sparse vegetation (Baddock et al., 2011; Kandakji et al., 2020). The strong southwesterly near-surface wind in both cases was able to entrain dust from likely dust source regions that were sparsely vegetated and made it available for long-range transport.

5. Discussion

Understanding the drivers of spring season (March–May) dust events in the southwestern US is important for monitoring and mitigating the effects of dust on water resources, agriculture, and air quality. We studied two dust events originating from geographically different dominant source areas of the Colorado Plateau and northern Chihuahuan Desert. The value of analyzing two case studies was to reveal how similar large-scale meteorology organizes dust events at two different dominant geographic source locations and evaluate the ability of the WRF-Chem model to represent these dust sources. Our large-scale meteorological analysis of the dust events indicates PJ and STJ interaction was a common upper-level meteorological feature before organization of the events. As our case studies encompassed dust emissions from across the Colorado Plateau and northern Chihuahuan Desert,

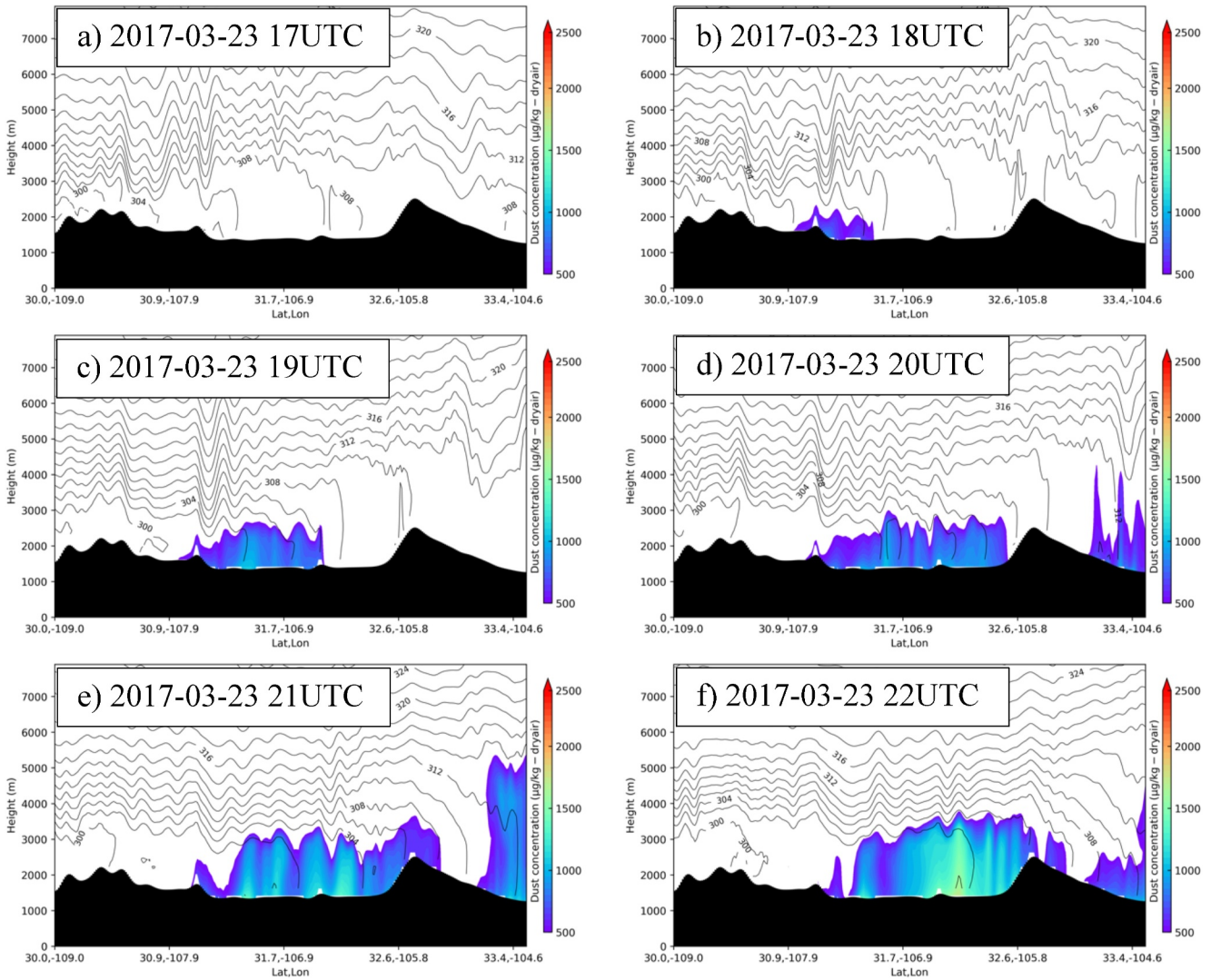


Figure 11. WRF-Chem simulated vertical cross-section of potential temperature (K) and dust concentration along CD (see Figure 1) at (a) 1700, (b) 1800, (c) 1900, (d) 2000, (e) 2100, and (f) 2200 UTC 23 March 2017.

this finding suggests the possible presence of upper-level jet interaction before dust events at different geographic locations in the Southwest. A previous study found similar jet interaction prior to a dust storm in the Southern High Plains (Kaplan et al., 2013) suggesting that upper-level jet interaction could be a meteorological precursor to

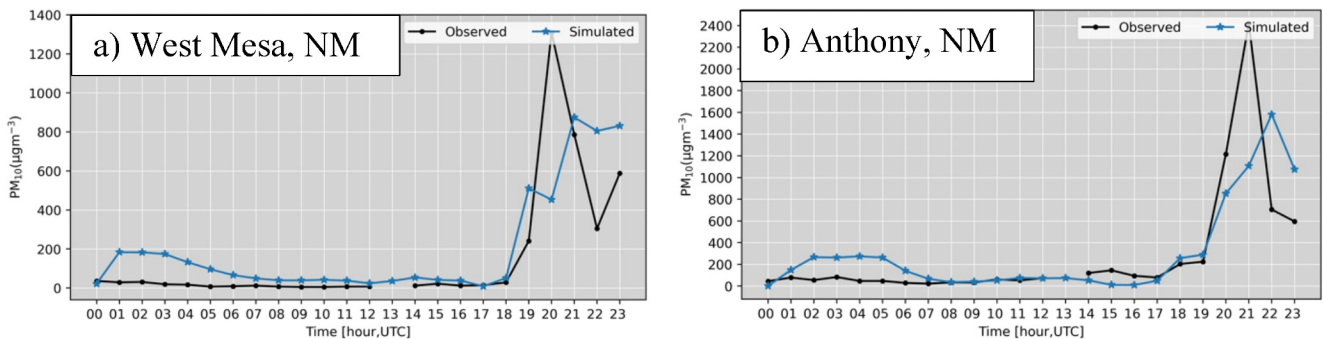


Figure 12. Hourly PM_{10} evolution at (a) West Mesa and (b) Anthony in New Mexico for 23 March 2017.

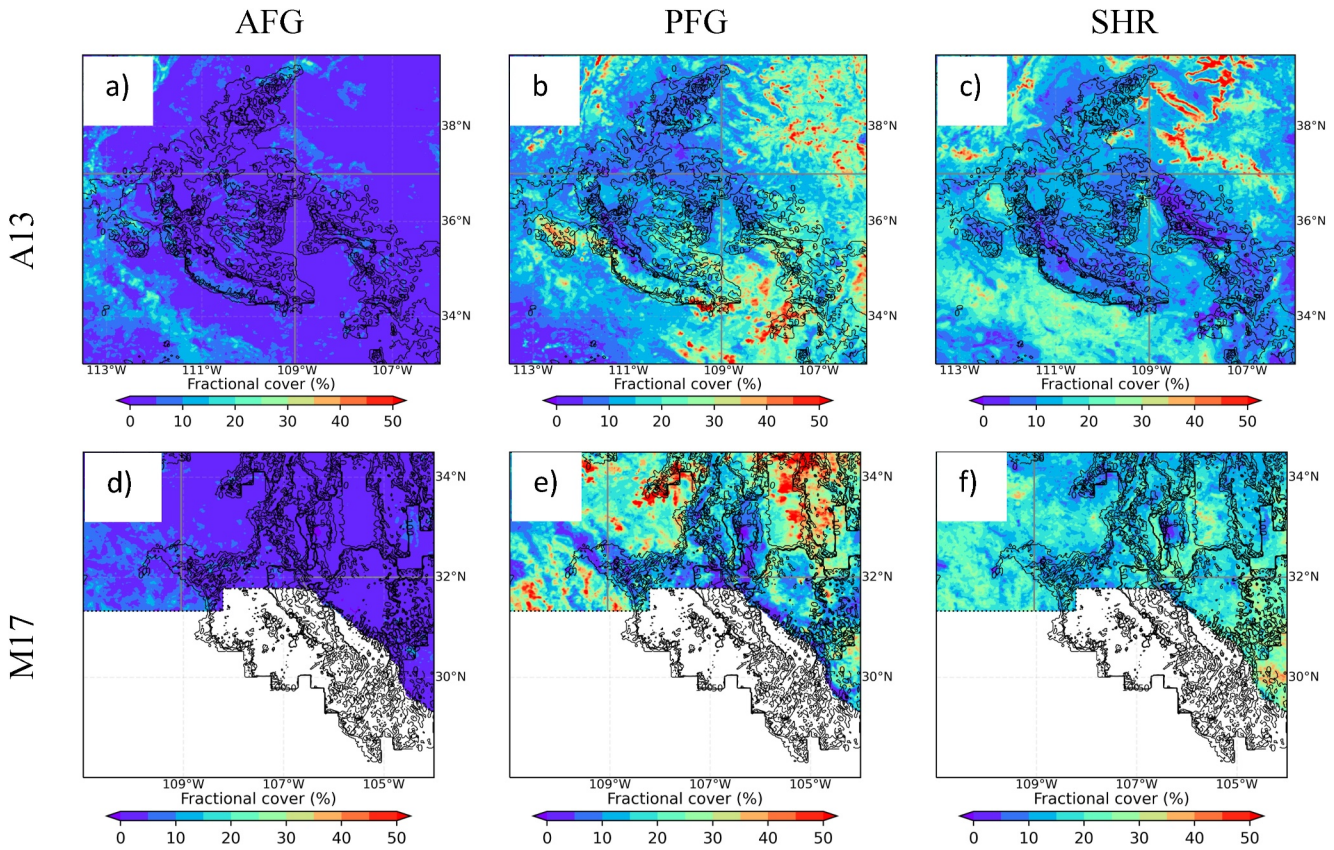


Figure 13. (a, b, c) Plant functional group annual fractional cover for 2012 and dust emission flux at 1800 UTC 16 April 2013 (black line contours). (d, e, f) Similar to Figures a, b, and c but for 2016 fractional cover and dust emission flux at 2000 UTC 23 March 2017.

dust events in the Southwest. A knowledge of such signals could be beneficial in dust storm operational forecasting and early warning systems to reduce the adverse operational impacts of blowing dust on landscapes, visibility for road traffic, air quality, and human health. For example, large-scale upper-level precursors were recently found to provide early warning of long-lived dust events in North Africa (Dhital et al., 2020; Orza et al., 2020). However, further investigation is needed with additional cases to assess the probability of and detailed dynamics of jet interaction before dust events are organized in the Southwest, to describe the nature of any mechanistic interactions, and to determine the implications for dust transport to snowpack in the CRB.

There remains a dearth of observational data sets in the Southwest US needed to rigorously test dust emission models (Webb et al., 2017). The Four Corners and northern Chihuahuan Desert (in Mexico) dust source regions are both sparsely monitored. Despite a large amount of dust being transported annually from the Colorado Plateau to the San Juan Mountains, there are no publicly accessible PM_{10} stations within the dust transport pathway. The only nearby PM_{10} observations are collected nearly 1° poleward of the San Juan Mountains. Nonetheless, assessment of our simulation results showed that WRF-Chem, with drag partition correction in the AFWA dust emission scheme, can simulate a general pattern of the spatiotemporal evolution of dust emission in geographically different source areas that contribute to dust-on-snow in the Southwest. Through comparison with satellite imagery of the dust plumes and plant functional group cover data sets, we assessed that the dust sources in the two geographic regions were well captured in our simulations. The pattern of simulated large dust emission flux in the southwestern Colorado Plateau, including the Little CRB, corresponds to a strong dust source region. Complementary research using similar and independent approaches has identified that the region between Flagstaff, Arizona and the Four Corners, including the Little CRB, are major dust sources on the Colorado Plateau (Hennen et al., 2022; Nauman et al., 2023). In the northern Chihuahuan Desert, our simulated pattern of large dust emission fluxes from unvegetated and poorly vegetated regions including dry playas is also consistent with previous studies (Baddock et al., 2011; Hennen et al., 2022). The large dust emitting regions in the simulations covering the

southwestern Colorado Plateau and northern Chihuahuan Desert also correspond to regions of measured large spring season sediment flux (Bergametti & Gillette, 2010), dust emission hotspots that contribute to blowing dust on highways (Tong et al., 2023) and large PM concentration (Hand et al., 2017). In the southwestern Colorado Plateau and northern Chihuahuan Desert, fine dust ($PM_{2.5}$) concentration peaks ($1.7\text{--}2.22\ \mu\text{g m}^{-3}$) are observed during the spring season (Hand et al., 2017).

Comparison of the simulated dust sources with plant functional group cover data enabled a novel assessment of the simulated dust sources and insights into the dust source area characteristics of our case study events. Not surprisingly, we found that the dust sources contributing to the largest dust emission fluxes in our simulations occurred on sparsely vegetated lands. Sparse vegetation is less effective at attenuating wind momentum and increases the probability of dust emission (Nauman et al., 2023; Webb et al., 2014). The patterns of large, simulated dust emission fluxes were collocated with a small fractional cover of annual and PFG, and shrubs. The variable annual precipitation regime across the Colorado Plateau and the Chihuahuan Desert impacts vegetation dynamics, which in turn modifies land surface roughness and changes the dynamics of dust emission and transport. Hence, future research could explore how regional drought impacts plant functional groups and land surface roughness and changes the dynamics of dust emission and transport.

Comparisons of the 2 km simulated meteorological and dust fields with point observational data sets for the two case studies also suggested reasonable model performance. We found some discrepancies in observed and simulated fields that warrant further attention. For example, the model underestimated the 10 m wind at the Flagstaff METAR station and underestimated the vertical wind profile at two sounding locations. At the Santa Teresa station, vertical profiles of simulated and observed wind were in close agreement up to 600 hPa but simulated winds were weaker above that. At the Flagstaff station, the near-surface winds were close to observations, but above 700 hPa, the simulated winds were weaker than observations. These discrepancies could be due to model performance or sub-grid scale heterogeneity and scale mismatches between the point-source station data and 2 km model grid (Mues et al., 2018; Yver et al., 2013; Zhang, Pu, & Zhang, 2013; Zhang, Sartelet, et al., 2013). They could also reflect inadequacies in the model initial conditions. Additionally, the model overestimated AOD at some locations. The simulation estimated dust emission and AOD occurred across a much larger portion of the study area than observations in both cases. The simulated AOD in the A13 was much more extensive than that of the M17 and coincided with much greater wind friction velocity. As the surface roughness (u_{*s}/U_h) was unchanged over the 2-day simulations, and modeled wind speed during the dust events corresponded with measurements, we interpret the cause of the overestimation in dust emission being due to the model assuming that sediment availability for emission is unlimited over time. This issue is a common problem among dust models (e.g., Parajuli et al., 2019; Shao et al., 2007) and an effective solution to parameterizing dynamic soil erodibility at the regional scale is very limited. In the 2017 case, we observed that the simulated PM_{10} peaked 1 hr after the observed PM_{10} peak. One plausible explanation for this lag is that the simulated wind was slightly weaker than the observed maximum wind approximately 2 hr prior to the observed PM_{10} peak. This may have resulted in less dust emission in the simulation and diminished PM_{10} .

Future research to evaluate and enhance the model performance, including better constraining dust-on-snow simulations and forecasting, would greatly benefit from improved monitoring of dust concentrations and dust emission fluxes within North American dust source regions. Additionally, there is a need to resolve large scale differences between numerical dust models (here 2 km resolution) and available observational data sets (point scale), which has been a challenging task (Haustein et al., 2015). As the already dry Southwest US is predicted to become even drier over the coming decades (Edwards et al., 2019), access to reliable dust monitoring data sets will be of critical importance for assessing the impacts and feedbacks among climate change, land uses, and land management on ecosystems and dust activity, dust-on-snow processes, and the implications of these interactions for agriculture water resources and dust mitigation (Webb et al., 2017). To effectively link these processes and evaluate the systems-levels interactions and impacts of dust-on-snow, it will be important to establish the accuracy of simulated dust emission fluxes and model representations of dust source area dynamics. Such efforts will necessarily shift the focus of dust model validation from almost exclusively testing advected dust concentrations and AOD to novel approaches that incorporate surface measurements and models of soil and vegetation, saltation mass fluxes, and dust emission.

The results from our two-spring season dust events simulations, and the improved simulation of a convective dust event in Arizona with the same drag-partition approach (LeGrand et al., 2023), give us confidence in the applicability of the Chappell and Webb (2016) albedo-based drag partition for simulating Southwest dust events under different meteorological and surface roughness conditions.

6. Conclusions

In this study, we investigated large-scale meteorological conditions leading to two spring-season Southwest US dust events. We found commonalities in upper-level meteorological circulations in these two cases. Our analyses revealed a common PJ and STJ interacting feature before the formation of dust events. When PJ and STJ merged resulting in a single unified jet, a strong mid-tropospheric flow developed. Within the near-surface boundary layer, a strong northeastward-directed pressure gradient developed just below and directly upstream of the exit region of the unified jet resulting in strong low-level winds capable of emitting dust from the source regions. The analyses suggest that PJ and STJ interaction could be a common upper-level meteorological precursor to Southwest dust events organized at different geographic locations. Such upper-level signals could be beneficial in operational dust storm forecasting and early warning systems to reduce the immediate adverse impact of dust events on human health and other environmental resources. Future work will extend and assess the probability of jet interaction before dust event formation in the Southwest with multiple cases and describe the nature of jet interaction and its role in dust emission and transport processes, most notably how these unified jets deepen the PBL mixed layers and accelerate the airflow.

We also simulated these two dust events using the WRF-Chem model with dynamic albedo-based drag partitioning within the AFWA dust emission scheme. We found that drag partition correction in the AFWA dust emission scheme can reasonably reproduce the spatiotemporal evolution of the dust plumes, which suggests its applicability in forecasting spring season dust events across different geographic and meteorological conditions in the Southwest. As the accurate simulation of dust events remains one of the major challenges in dust emission and transport modeling, the ability of albedo-model to simulate dust emission and transport in different geographic and meteorological conditions is beneficial for various applications, including operational dust forecasting, regional climate modeling, dust cycles analyses, etc. Future work could use a similar model configuration to simulate other dust events for its potential wider use in operational forecasting and research.

Data Availability Statement

The observation and reanalysis data sets are freely available. ERA5 reanalysis data are available from Copernicus Climate Data Store (Hersbach et al., 2020a, 2020b) [Dataset]. METAR data are available from the IOWA State University website (METAR) [Dataset]. MODIS-Aqua images are available from the NASA Worldview platform (NASA Worldview) [Dataset]. MODIS AOD data are available from the NASA Earth Data website (MODIS) [Dataset], while PM₁₀ data are available from the US EPA website (PM10) [Dataset]. The soundings are available from the University of Wyoming website (Sounding) [Dataset] and the WRF-Chem simulations results are reproducible. A detailed description of getting MODIS albedo data to modify the AFWA code is provided in LeGrand et al. (2023). Plant functional group data are available from the Google Earth Engine and detailed description of getting these data is available in RAP website (RAP, 2023) [Dataset]. Python software package was used to make figures (PYTHON, 2022) [Software].

References

- Achakulwisut, P., Shen, L., & Mickley, L. J. (2017). What controls springtime fine dust variability in the western United States? Investigating the 2002–2015 increase in fine dust in the US Southwest. *Journal of Geophysical Research: Atmospheres*, 122(22), 12449–12467. <https://doi.org/10.1002/2017JD027208>
- Adhikari, P., & Mejia, J. F. (2022). Impact of transported dust aerosols on precipitation over the Nepal Himalayas using convection-permitting WRF-Chem simulation. *Atmospheric Environment: X*, 15, 15. <https://doi.org/10.1016/j.aeaoa.2022.100179>
- Baddock, M. C., Gill, T. E., Bullard, J. E., Acosta, M. D., & Rivera, N. I. R. (2011). Geomorphology of the Chihuahuan Desert based on potential dust emissions. *Journal of Maps*, 7(1), 249–259. <https://doi.org/10.4113/jom.2011.1178>
- Bergametti, G., & Gillette, D. A. (2010). Aeolian sediment fluxes measured over various plant/soil complexes in the Chihuahuan desert. *Journal of Geophysical Research*, 115(F3), F03044. <https://doi.org/10.1029/2009JF001543>
- Bohren, C. F., & Huffman, D. R. (2007). *Absorption and scattering of light by small particles* (p. 530). John Wiley & Sons, Ltd. <https://doi.org/10.1002/9783527618156>
- Chappell, A., & Webb, N. P. (2016). Using albedo to reform wind erosion modelling, mapping and monitoring. *Aeolian Research*, 23, 63–78. <https://doi.org/10.1016/j.aeolia.2016.09.006>

Acknowledgments

We thank three anonymous reviewers for their constructive comments, which helped to improve the manuscript. The funding for this work is supported by the National Aeronautics and Space Administration Grant 80NSSC20K1673. This research used resources provided by the SCINet project of the United States Department of Agriculture Agricultural Research Service (ARS), ARS project number 0500-00093-001-00-D to perform WRF-Chem simulations. Any use of trade, firm or product names is for descriptive purposes only and does not imply endorsement by the U.S. Government. During the development of the manuscript NPW and AC were in receipt of funding from the National Science Foundation (EAR-1853853) and Natural Environmental Research Council (NE/T002263/1, NERC/DMP-2634).

- Chappell, A., Webb, N. P., Guerschman, J. P., Thomas, D. T., Mata, G., Handcock, R. N., et al. (2018). Improving ground cover monitoring for wind erosion assessment using MODIS BRDF parameters. *Remote Sensing of Environment*, *204*, 756–768. <https://doi.org/10.1016/j.rse.2017.09.026>
- Dhital, S., Kaplan, M. L., Orza, J. A. G., & Fiedler, S. (2020). Atmospheric dynamics of a Saharan dust outbreak over Mindelo, Cape Verde Islands, preceded by Rossby wave breaking: Multiscale observational analyses and simulations. *Journal of Geophysical Research: Atmospheres*, *125*(18), 1–22. <https://doi.org/10.1029/2020JD032975>
- Dhital, S., Kaplan, M. L., Orza, J. A. G., & Fiedler, S. (2021). Poleward transport of African dust to the Iberian Peninsula organized by a barrier jet and hydraulic jumps: Observations and high-resolution simulation analyses. *Atmospheric Environment*, *261*, 118574. <https://doi.org/10.1016/j.atmosenv.2021.118574>
- Duniway, M. C., Pfennigwerth, A. A., Fick, S. E., Nauman, T. W., Belnap, J., & Barger, N. N. (2019). Wind erosion and dust from US drylands: A review of causes, consequences, and solutions in a changing world. *Ecosphere*, *10*(3). <https://doi.org/10.1002/ecs2.2650>
- Edwards, B. L., Webb, N. P., Brown, D. P., Elias, E., Peck, D. E., Pierson, F. B., et al. (2019). Climate change impacts on wind and water erosion on US rangelands. *Journal of Soil and Water Conservation*, *74*(4), 405–418. <https://doi.org/10.2489/jswc.74.4.405>
- Ek, M. B., Mitchell, K. E., Lin, Y., Rogers, E., Grunmann, P., Koren, V., et al. (2003). Implementation of Noah land surface model advances in the National Centers for Environmental Prediction operational mesoscale Eta model. *Journal of Geophysical Research*, *108*(D22), 2002JD003296. <https://doi.org/10.1029/2002JD003296>
- Evan, A. T., Porter, W., Clemesha, R., Kuwano, A., & Frouin, R. (2022). Measurements of a dusty density current in the western Sonoran desert. *Journal of Geophysical Research: Atmospheres*, *127*(8), 1–22. <https://doi.org/10.1029/2021JD035830>
- Fécan, F., Marticorena, B., & Bergametti, G. (1999). Parametrization of the increase of the Aeolian erosion threshold wind friction velocity due to soil moisture for arid and semi-arid areas. *Annales Geophysicae*, *17*(1), 149–157. <https://doi.org/10.1007/s00585-999-0149-7>
- Gallagher, A. R., LeGrand, S. L., Hodgdon, T. S., & Letcher, T. W. (2022). *Simulating environmental conditions for southwest United States convective dust storms using the Weather Research and Forecasting model v4.1*. ERDC TR-22-11. U.S. Army Engineer Research and Development Center. <https://doi.org/10.21079/11681/44963>
- Ginoux, P., Chin, M., Tegen, I., Prospero, J. M., Holben, B., Dubovik, O., & Lin, S.-J. (2001). Sources and distributions of dust aerosols simulated with the GOCART model. *Journal of Geophysical Research*, *106*(D17), 20255–20273. <https://doi.org/10.1029/2000JD000053>
- Grell, G. A., & Dévényi, D. (2002). A generalized approach to parameterizing convection combining ensemble and data assimilation techniques. *Geophysical Research Letters*, *29*(14), 10–13. <https://doi.org/10.1029/2002GL015311>
- Grell, G. A., Peckham, S. E., Schmitz, R., McKeen, S. A., Frost, G., Skamarock, W. C., & Eder, B. (2005). Fully coupled “online” chemistry within the WRF model. *Atmospheric Environment*, *39*(37), 6957–6975. <https://doi.org/10.1016/j.atmosenv.2005.04.027>
- Hand, J. L., Gill, T. E., & Schichtel, B. A. (2017). Spatial and seasonal variability in fine mineral dust and coarse aerosol mass at remote sites across the United States. *Journal of Geophysical Research*, *122*(5), 3080–3097. <https://doi.org/10.1002/2016JD026290>
- Hand, J. L., Gill, T. E., & Schichtel, B. A. (2019). Urban and rural coarse aerosol mass across the United States: Spatial and seasonal variability and long-term trends. *Atmospheric Environment*, *218*(July), 117025. <https://doi.org/10.1016/j.atmosenv.2019.117025>
- Hausstein, K., Washington, R., King, J., Wiggs, G., Thomas, D. S. G., Eckardt, F. D., et al. (2015). Testing the performance of state-of-the-art dust emission schemes using DO4Models field data. *Geoscientific Model Development*, *8*(2), 341–362. <https://doi.org/10.5194/gmd-8-341-2015>
- Hennen, M., Chappell, A., Edwards, B. L., Faist, A. M., Kandakji, T., Baddock, M. C., et al. (2022). A North American dust emission climatology (2001–2020) calibrated to dust point sources from satellite observations. *Aeolian Research*, *54*, 100766. <https://doi.org/10.1016/j.aeolia.2021.100766>
- Hersbach, H., Bell, B., Berrisford, P., Hirahara, S., Horányi, A., Muñoz-Sabater, J., et al. (2020a). The ERA5 global reanalysis. *Quarterly Journal of the Royal Meteorological Society*, *146*(730), 1999–2049. <https://doi.org/10.1002/qj.3803>
- Hersbach, H., Bell, B., Berrisford, P., Hirahara, S., Horányi, A., Muñoz-Sabater, J., et al. (2020b). ERA-5 reanalysis data [Dataset]. <https://www.ecmwf.int/en/forecasts/datasets/reanalysis-datasets/era5>
- Iacono, M. J., Delamere, J. S., Mlawer, E. J., Shephard, M. W., Clough, S. A., & Collins, W. D. (2008). Radiative forcing by long-lived greenhouse gases: Calculations with the AER radiative transfer models. *Journal of Geophysical Research*, *113*(13), 1–8. <https://doi.org/10.1029/2008JD009944>
- Jones, M. O., Allred, B. W., Naugle, D. E., Maestas, J. D., Donnelly, P., Metz, L. J., et al. (2018). Innovation in rangeland monitoring: Annual, 30 m, plant functional type percent cover maps for US Rangelands, 1984–2017. *Ecosphere*, *9*(9), e02430. <https://doi.org/10.1002/ecs2.2430>
- Kandakji, T., Gill, T. E., & Lee, J. A. (2020). Identifying and characterizing dust point sources in the southwestern United States using remote sensing and GIS. *Geomorphology*, *353*, 107019. <https://doi.org/10.1016/j.geomorph.2019.107019>
- Kaplan, M. L., Vellore, R. K., Lewis, J. M., Underwood, S. J., Pauley, P. M., Martin, J. E., et al. (2013). Subtropical-polar jet interactions in Southern Plains dust storms. *Journal of Geophysical Research: Atmospheres*, *118*(23), 12893–12914. <https://doi.org/10.1002/2013JD020345>
- Kort, W. (2013). *Climate change impacts on agriculture in the Rio Grande River Basin*. School of Freshwater Sciences: Center for Water Policy at University of Wisconsin. Retrieved from http://uwm.edu/centerforwaterpolicy/wp-content/uploads/sites/170/2013/10/Rio-Grande_Agriculture_Final.pdf
- LeGrand, S. L., Letcher, T. W., Okin, G. S., Webb, N. P., Gallagher, A. R., Dhital, S., et al. (2023). Application of a satellite-retrieved sheltering parameterization (v1.0) for dust event simulation with WRF-Chem v4.1. *Geoscientific Model Development*, *16*(3), 1009–1038. <https://doi.org/10.5194/gmd-16-1009-2023>
- LeGrand, S. L., Polashenski, C., Letcher, T. W., Creighton, G. A., Peckham, S. E., & Cetola, J. D. (2019). The AFWA dust emission scheme for the GOCART aerosol model in WRF-Chem v3.8.1. *Geoscientific Model Development*, *12*(1), 131–166. <https://doi.org/10.5194/gmd-12-131-2019>
- Lei, H., & Wang, J. X. L. (2014). Observed characteristics of dust storm events over the western United States using meteorological, satellite, and air quality measurements. *Atmospheric Chemistry and Physics*, *14*(15), 7847–7857. <https://doi.org/10.5194/acp-14-7847-2014>
- Li, J., Okin, G. S., McKenzie Skiles, S., & Painter, T. H. (2013). Relating variation of dust on snow to bare soil dynamics in the western United States. *Environmental Research Letters*, *8*(4), 044054. <https://doi.org/10.1088/1748-9326/8/4/044054>
- METAR. (2022). METAR data [Dataset]. <https://mesonet.agron.iastate.edu/request/download.phtml>
- Michaels, M. L., Letcher, T. W., LeGrand, S. L., Webb, N. P., & Putnam, J. B. (2022). *Implementation of an albedo-based drag partition into the WRF-Chem v4.1 AFWA dust emission module*. Cold Regions Research and Engineering Laboratory. <https://hdl.handle.net/11681/42782>
- MODIS. (2022). MODIS AOD data [Dataset]. <https://ladsweb.modaps.eosdis.nasa.gov>
- Mues, A., Lauer, A., Lupascu, A., Rupakheti, M., Kuik, F., & Lawrence, M. G. (2018). WRF and WRF-Chem v3.5.1 simulations of meteorology and black carbon concentrations in the Kathmandu Valley. *Geoscientific Model Development*, *11*(6), 2067–2091. <https://doi.org/10.5194/gmd-11-2067-2018>

- Nakanishi, M., & Niino, H. (2004a). Development of an improved turbulence closure model for the atmospheric boundary layer. *Journal of the Meteorological Society of Japan*, 87(5), 895–912. <https://doi.org/10.2151/jmsj.87.895>
- Nakanishi, M., & Niino, H. (2004b). An improved Mellor–Yamada Level-3 Model with condensation physics: Its design and verification. *Boundary-Layer Meteorology*, 112, 1–31. <https://doi.org/10.1023/B:BOUN.0000020164.04146.98>
- NASA Worldview. (2022). MODIS-Aqua images [Dataset]. <https://www.earthdata.nasa.gov/worldview>
- Nauman, T. W., Munson, S. M., Dhital, S., Webb, N. P., & Duniway, M. C. (2023). Synergistic soil, land use, and climate influences on wind erosion on the Colorado Plateau: Implications for management. *Science of the Total Environment*, 893(December 2022), 164605. <https://doi.org/10.1016/j.scitotenv.2023.164605>
- Oaida, C. M., Xue, Y., Flanner, M. G., Skiles, S. M. K., De Sales, F., & Painter, T. H. (2015). Improving snow albedo processes in WRF/SSiB regional climate model to assess impact of dust and black carbon in snow on surface energy balance and hydrology over western US. *Journal of Geophysical Research*, 120(8), 3228–3248. <https://doi.org/10.1002/2014JD022444>
- Orza, J. A. G., Dhital, S., Fiedler, S., & Kaplan, M. L. (2020). Large scale upper-level precursors for dust storm formation over North Africa and poleward transport to the Iberian Peninsula. Part I: An observational analysis. *Atmospheric Environment*, 237, 117688. <https://doi.org/10.1016/j.atmosenv.2020.117688>
- Painter, T. H., Deems, J. S., Belnap, J., Hamlet, A. F., Landry, C. C., & Udall, B. (2010). Response of Colorado River runoff to dust radiative forcing in snow. *Proceedings of the National Academy of Sciences of the United States of America*, 107(40), 17125–17130. <https://doi.org/10.1073/PNAS.0913139107>
- Parajuli, S. P., Stenchikov, G. L., Ukhov, A., & Kim, H. (2019). Dust emission modeling using a new high-resolution dust source function in WRF-Chem with implications for air quality. *Journal of Geophysical Research: Atmospheres*, 124(17–18), 10109–10133. <https://doi.org/10.1029/2019JD030248>
- PM10. (2022). PM₁₀ data [Dataset]. https://aqs.epa.gov/aqsweb/airdata/download_files.html
- PYTHON. (2022). Python matplotlib software package [Software]. <https://matplotlib.org/>
- Rahimi, S., Liu, X., Zhao, C., Lu, Z., & Lebo, Z. J. (2020). Examining the atmospheric radiative and snow-darkening effects of black carbon and dust across the Rocky Mountains of the United States using WRF-Chem. *Atmospheric Chemistry and Physics*, 20(18), 10911–10935. <https://doi.org/10.5194/acp-20-10911-2020>
- RAP. (2023). Plant functional groups data [Dataset]. <https://rangelands.app/products/>
- Raupach, M. R. (1992). Drag and drag partition on rough surfaces. *Boundary-Layer Meteorology*, 60(4), 374–396. <https://doi.org/10.1007/bf00155203>
- Raupach, M. R., & Lu, H. (2004). Representation of land-surface processes in aeolian transport models. *Environmental Modelling & Software*, 19(2), 93–112. [https://doi.org/10.1016/S1364-8152\(03\)00113-0](https://doi.org/10.1016/S1364-8152(03)00113-0)
- Schaaf, C., & Wang, Z. (2021). MODIS/Terra+Aqua BRDF/albedo model parameters daily L3 Global - 500m V061. NASA EOSDIS Land Processes Distributed Active Archive Center. <https://doi.org/10.5067/MODIS/MCD43A1.061>
- Shao, Y., Leys, J. F., McTainsh, G. H., & Tews, K. (2007). Numerical simulation of the October 2002 dust event in Australia. *Journal of Geophysical Research*, 112(D8), D08207. <https://doi.org/10.1029/2006JD007767>
- Skamarock, W. C., Klemp, J. B., Dudhia, J., Gill, D. O., Liu, Z., Berner, J., et al. (2019). A Description of the advanced research WRF model version 4.1. <https://doi.org/10.5065/1dfh-6p97>
- Skiles, S. M., Painter, T. H., Belnap, J., Holland, L., Reynolds, R. L., Goldstein, H. L., & Lin, J. (2015). Regional variability in dust-on-snow processes and impacts in the Upper Colorado River Basin. *Hydrological Processes*, 29(26), 5397–5413. <https://doi.org/10.1002/hyp.10569>
- Skiles, S. M. K., & Painter, T. (2017). Daily evolution in dust and black carbon content, snow grain size, and snow albedo during snowmelt, Rocky Mountains, Colorado. *Journal of Glaciology*, 63(237), 118–132. <https://doi.org/10.1017/jog.2016.125>
- Skiles, S. M. K., & Painter, T. H. (2018). Assessment of radiative forcing by light-absorbing particles in snow from in situ observations with radiative transfer modeling. *Journal of Hydrometeorology*, 19(8), 1397–1409. <https://doi.org/10.1175/JHM-D-18-0072.1>
- Solomos, S., Kalivitis, N., Mihalopoulos, N., Amiridis, V., Kouvarakis, G., Gkikas, A., et al. (2018). From tropospheric folding to Khamsin and Foehn winds: How atmospheric dynamics advanced a record-breaking dust episode in Crete. *Atmosphere*, 9(7), 240. <https://doi.org/10.3390/atmos9070240>
- Sounding. (2022). Upper air sounding data [Dataset]. <https://weather.uwyo.edu/upperair/sounding.html>
- Thiel, A. (2013). *Climate change impacts on agriculture in the Colorado River Basin*. School of Freshwater Sciences: Center for Water Policy at University of Wisconsin. Retrieved from https://uwm.edu/centerforwaterpolicy/wp-content/uploads/sites/170/2013/10/Colorado_Agriculture_Final.pdf
- Thompson, G., Field, P. R., Rasmussen, R. M., & Hall, W. D. (2008). Explicit forecasts of winter precipitation using an improved bulk microphysics scheme. Part II: Implementation of a new snow parameterization. *Monthly Weather Review*, 136(12), 5095–5115. <https://doi.org/10.1175/2008MWR2387.1>
- Tong, D. Q., Gill, T. E., Sprigg, W. A., Van Pelt, R. S., Baklanov, A. A., Barker, B. M., et al. (2023). Health and safety effects of airborne soil dust in the Americas and beyond. *Reviews of Geophysics*, 61(2), e2021RG000763. <https://doi.org/10.1029/2021RG000763>
- Ukhov, A., Ahmadov, R., Grell, G., & Stenchikov, G. (2021). Improving dust simulations in WRF-Chem v4.1.3 coupled with the GOCART aerosol module. *Geoscientific Model Development*, 14(1), 473–493. <https://doi.org/10.5194/gmd-14-473-2021>
- Webb, N. P., Chappell, A., LeGrand, S. L., Ziegler, N. P., & Edwards, B. L. (2020). A note on the use of drag partition in aeolian transport models. *Aeolian Research*, 42, 100560. <https://doi.org/10.1016/j.aeolia.2019.100560>
- Webb, N. P., Okin, G. S., & Brown, S. (2014). The effect of roughness elements on wind erosion: The importance of surface shear stress distribution. *Journal of Geophysical Research: Atmospheres*, 119(10), 6066–6084. <https://doi.org/10.1002/2014JD021491>
- Webb, N. P., Van Zee, J. W., Karl, J. W., Herrick, J. E., Courtright, E. M., Billings, B. J., et al. (2017). Enhancing wind erosion monitoring and assessment for US rangelands. *Rangelands*, 39(3–4), 85–96. <https://doi.org/10.1016/j.rala.2017.04.001>
- Yver, C. E., Graven, H. D., Lucas, D. D., Cameron-Smith, P. J., Keeling, R. F., & Weiss, R. F. (2013). Evaluating transport in the WRF model along the California coast. *Atmospheric Chemistry and Physics*, 13(4), 1837–1852. <https://doi.org/10.5194/acp-13-1837-2013>
- Zhang, H., Pu, Z., & Zhang, X. (2013). Examination of errors in near-surface temperature and wind from WRF numerical simulations in regions of complex terrain. *Weather and Forecasting*, 28(3), 893–914. <https://doi.org/10.1175/WAF-D-12-00109.1>
- Zhang, Y., Sartelet, K., Wu, S.-Y., & Seigneur, C. (2013). Application of WRF/Chem-MADRID and WRF/Polphemus in Europe – Part 1: Model description, evaluation of meteorological predictions, and aerosol–meteorology interactions. *Atmospheric Chemistry and Physics*, 13(14), 6807–6843. <https://doi.org/10.5194/acp-13-6807-2013>
- Zhao, C., Liu, X., Leung, L. R., Johnson, B., McFarlane, S. A., Gustafson, W. I., Jr., et al. (2010). The spatial distribution of mineral dust and its shortwave radiative forcing over North Africa: Modeling sensitivities to dust emissions and aerosol size treatments. *Atmospheric Chemistry and Physics*, 10(18), 8821–8838. <https://doi.org/10.5194/acp-10-8821-2010>